International Journal of Plasticity 72 (2015) 91–126

Contents lists available at ScienceDirect

International Journal of Plasticity

journal homepage: www.elsevier.com/locate/ijplas

A quasistatic implementation of the concurrent atomistic-continuum method for FCC crystals

Shuozhi Xu [a, *], Rui Che [b], Liming Xiong [c], Youping Chen [b], David L. McDowell [a, d]

[a] GWW School of Mechanical Engineering, Georgia Institute of Technology, Atlanta, GA 30332-0405, USA
[b] Department of Mechanical and Aerospace Engineering, University of Florida, Gainesville, FL 32611-6250, USA
[c] Department of Aerospace Engineering, Iowa State University, Ames, IA 50011, USA
[d] School of Materials Science and Engineering, Georgia Institute of Technology, Atlanta, GA 30332-0245, USA

ARTICLE INFO

Article history:
Received 31 October 2014
Received in revised form 20 April 2015
Available online 30 May 2015

Keywords:
Concurrent atomistic-continuum method
A. Dislocations
B. Metallic material
C. Finite elements
C. Numerical algorithms

ABSTRACT

In recent years, numerous partitioned-domain methods have been developed to describe dislocation behavior at length scales that are usually inaccessible to most classical atomistic methods. These methods retain full atomistic detail in regions of interest while using a continuum description to reduce the computational burden elsewhere. In most of these methods, however, lattice defects in the continuum are either implemented via constitutive relations, lattice elasticity with dislocation field interactions, or are not permitted at all. In such approaches, the transit of dislocations across the atomistic/continuum interface appeals to approximate heuristics intended to minimize the effects of the interface due to the change from atomistic to continuum degrees of freedom. The concurrent atomistic-continuum (CAC) method, originally developed for addressing dynamic dislocation behavior by Xiong et al. (2011), permits dislocations to propagate in a continuum domain that employs a piecewise continuous finite element description with interelement displacement discontinuities. The method avoids ghost forces at interface between atomistically resolved and coarse-grained domains. CAC has subsequently been used to investigate complex dislocation behavior in face-centered cubic (FCC) metals (Xiong et al., 2012b,a,c, 2015). In this paper, we propose a quasistatic 3-D method to carry out sequential energy-minimized simulations at 0 K. This facilitates study of structure evolution along minimum energy pathways, avoiding over-driven conditions of high rate molecular dynamics. Parallelization steps in code implementation are described. Applications are presented for the quasistatic CAC method in FCC metal plasticity. Comparisons are made with a fully-resolved atomistic method for generalized stacking fault energy, core structure and stress field of a single 60° mixed type dislocation, surface indentation, and 60° mixed type dislocation migration through the interface between atomistic and coarse-grained domains. It is shown that 3-D CAC simulations are useful in substantially reducing the number of degrees of freedom while preserving key characteristics of dislocation structure, stacking faults, and plasticity, including the net Burgers vector and long range fields of interacting dislocations.

* Corresponding author.
E-mail address: shuozhixu@gatech.edu (S. Xu).

http://dx.doi.org/10.1016/j.ijplas.2015.05.007
0749-6419/

1. Introduction

Metal plasticity is a multiscale phenomenon that is manifested by irreversible microstructure rearrangement associated with nucleation, multiplication, interaction, and migration of dislocations (McDowell, 2010). Long range field interactions between dislocations are extremely important to describe, along with the dissociated character of partial dislocations. The former necessitates large solution scales, while the latter demands treatment of core effects using accurate underlying interatomic potentials. Metal plasticity therefore requires concurrent coupling across various scales. While methods such as molecular dynamics (MD) and discrete dislocation dynamics (DDD) have been widely employed for problems at respective spatial scales involving core effects and long range fields, efforts have been made to concurrently bridge the discrete and continuous descriptions, two fundamentally different approaches (Rudd and Broughton, 2000). Chen et al. (2011) reviewed the theoretical foundations of coarse graining methods and analyzed several representative coarse graining models. A review of 14 concurrent multiscale modeling methods is presented by Miller and Tadmor (2009), and is further summarized by Tadmor and Miller (2012).

Concurrent multiscale methods can be categorized as hierarchical and partitioned-domain methods, where the latter divides the system into atomistic and continuum domains. An example of a partitioned-domain method is the coupled atomistic and discrete dislocation (CADD) method (Shilkrot et al., 2004). The CADD model permits the transfer of dislocations across the interface between the atomistic and continuum domains. It has been employed to incorporate long range fields of dislocation pileups to study the impingement of dislocations on symmetric tilt grain boundaries (GB) in Al by Dewald and Curtin (2007a,b,2011). However, CADD is restricted in that heuristic, *ad hoc* treatments are introduced to pass dislocations through the continuum–atomistic interface; dislocations are detected on one side of the interface and inserted into the other. Moreover, the treatment of curved dislocations of mixed character that might cross domain interfaces is problematic.

Another concurrent atomistic-continuum approach is the quasicontinuum (QC) method (Tadmor et al., 1996). The QC method uses the change of deformation gradient to distinguish domains where full atomistic resolution is required from those where the deformation field varies more smoothly. Representative atoms (repatom) are employed to reduce the degrees of freedom to a small fraction of those required in fully resolved atomistic simulations. The system energy, based on the repatoms, is minimized so that the lattice statics at 0 K is reproduced (Miller and Tadmor, 2002). Recently, the QC method has been extended to include a dynamic, finite temperature formulation (Dupuy et al., 2005; Kulkarni et al., 2008; Tadmor et al., 2013). In such approaches, it is difficult to avoid introduction of a ghost force at the atomistic/continuum interface. Also, since the defects can only nucleate and migrate within the fully atomistic domain, *ad hoc* criteria are needed to assist in adaptive mesh refinement (Shimokawa et al., 2009).

To the authors' knowledge, most partitioned-domain methods, including CADD and QC, treat the continuum domain such that lattice dislocations are either implemented via elastic constitutive relations, or not permitted at all. This motivated development of a new partitioned-domain method called the concurrent atomistic-continuum (CAC) method that employs piecewise continuous first order shape function and interpolation function within elements and admits displacement discontinuities between elements (Xiong et al., 2012a). Boundary layers are employed near element interface to accommodate additional inhomogeneous deformation. In this way, nucleation of dislocations and transport between fully resolved atomistic and coarse-grained domains are permitted, without requiring heuristic rules or overlapping pad regions. Ghost forces are avoided at such interfaces.

The theoretical foundation of the CAC method is the atomistic field theory (AFT). It is rooted in micromorphic theory, where a local density function is used to connect the micromorphic theory and molecular dynamics, in which a crystalline material is viewed as a continuous collection of lattice points, while embedded within each point is a unit cell with a group of discrete atoms (Chen and Lee, 2005). The same balance equations for both fully resolved atomistic and coarse-grained continuum domains are employed to compute the properties of general crystals. In the continuum domain, the interatomic potential serves as the only constitutive relation. The AFT was originally designed with multi-atom crystalline materials in mind (Chen and Lee, 2003a,b), and CAC has been applied on strontium titanate (Yang et al., 2013b; Yang and Chen, 2015) and phonon properties of the 1-D polyatomic crystals (Xiong et al., 2014a).

For monoatomic crystalline materials, each primitive unit cell contains only one atom. Xiong et al. (2011) performed CAC simulations to reproduce the complex dislocation phenomena in FCC metals such as dislocation nucleation/migration and formation of multiple stacking fault ribbons. Deng et al. (2010) and Deng and Chen (2013) studied the wave and crack propagation, as well as the impact fracture in an ideal brittle material. More recently, the embedded atom method (EAM) potential was incorporated in CAC simulations to study more general dislocation behavior such as migration of curved dislocations, formation of leading and trailing partial dislocations, dislocation loop coalescence, dislocation–phonon interactions, and dislocation–void interactions in pure FCC crystals (Xiong et al., 2012b,c,a, 2014b, 2015).

The objective of the present work is to briefly review the basic formulations in AFT, formulate a new quasistatic 3-D CAC method that employs sequential energy minimization for problems involving dislocation migration and interaction with domain interface, detail the numerical implementation, and demonstrate its applicability to metal plasticity involving arrays of dislocations in pure FCC crystals. Since the quasistatic CAC method facilitates exploration of structure evolution along minimum energy pathways, in contrast to over-driven MD simulations at high rates, we explore how the quasistatic CAC method provides largely satisfactory predictive results for benchmark simulations at a much lower computational cost than

the fully atomistic version of the same models. In addition to the quasistatic implementation of the original CAC method, new elements are introduced to improve the accuracy in modeling generalized stacking fault energy in the coarse-grained domain. To our knowledge, this is the first coarse-grained atomistic approach that can approximate dislocation core level effects without adaptive mesh refinement to the atomic scale.

2. Basic formulations

2.1. Governing equation

Within the framework of atomic N-body dynamics, Chen (2009) formulated the microscopic balance equations of the instantaneous mass, linear momentum, and internal energy. Fundamentally different from the form of coarse-grained particle models, the governing equations in AFT are expressed in terms of local densities (Chen et al., 2011). While the balance equations can be expressed in terms of either Eulerian or Lagrangian coordinates, we follow the work of Chen (2009) and adopt Eulerian coordinates in this paper. For a monoatomic crystal, assuming that the temperature gradient is negligible and there is no external force density, the governing equation in the dynamic CAC method subject to the assumption of homogeneous temperature is (Chen and Lee, 2005)

$$\rho\ddot{\mathbf{r}} - \mathbf{f}_{\text{int}} = \mathbf{0} \tag{1}$$

where ρ is the microscopic local mass density, $\mathbf{r}$ is the physical space coordinates, $\mathbf{f}_{\text{int}}$ is the internal force density, and the superposed dots denote the material time derivative. Note that the local density is defined as the time-interval averages of instantaneous quantities, as in MD method, rather than the ensemble averages employed in statistical mechanics. The local density is continuous in the physical space up to the point of structural instability (e.g., dislocation nucleation or fracture).

While it appears straightforward to apply this equation to solve the dynamic problem for any prescribed homogeneous temperature, it is difficult to construct a uniform temperature formulation for both atomistic and continuum domains, and is a matter of ongoing development. In this paper, we propose a quasistatic analog of the CAC method, similar in character to molecular statics (MS). At 0 K, coarse-grained MS simulations are useful for probing the energy landscape of the material system, and help to distinguish structural contributions to mechanical properties from common overdriven conditions associated with very high strain rates in MD and/or thermal fluctuation due to finite temperature. In the following sections, instead of adopting Eq. (1) directly, we use it to derive the equivalent nodal force and energy, forming the basis for the energy minimization procedure.

2.2. Continuum quantities from atomistics

In the continuum, the instantaneous mechanical variables ρ, $\ddot{\mathbf{r}}$, and $\mathbf{f}_{\text{int}}$ are defined at each material point $\mathbf{r}$ in physical space. In an atomistic description, however, their values must be obtained in terms of the discrete properties defined for each atom in the system (e.g., position, momentum, and energy) at atomic site $\mathbf{R}$ in phase space. In AFT, Chen and Lee (2005) propose that the phase space and physical space descriptions can be linked by the localization function δ, i.e.,

$$\rho(\mathbf{r})\ddot{\mathbf{r}} = \sum_{k=1}^{N_{\text{atom}}} \delta\left(\mathbf{r} - \mathbf{R}^k\right) m^k \ddot{\mathbf{R}}^k \tag{2}$$

$$\mathrm{f}_{\text{int}}(\mathbf{r}) = \sum_{k=1}^{N_{\text{atom}}} \delta\left(\mathbf{r} - \mathbf{R}^k\right) \mathbf{F}^k \tag{3}$$

where N_{atom} is the number of atoms, δ-function has units of inverse volume, $\mathbf{F}^k$ is the total atomic force acting on atom k, having mass m^k and position $\mathbf{R}^k$. While δ-function can be either a Dirac δ-function or a distribution function, it must satisfy that over the simulation domain Ω,

$$\int_{\Omega(\mathbf{r})} \delta\left(\mathbf{r} - \mathbf{R}^k\right) \mathrm{d}\Omega(\mathbf{r}) = 1. \tag{4}$$

In this paper, we employ a Dirac δ-function, i.e.,

$$\delta\left(\mathbf{r} - \mathbf{R}^k\right) = \begin{cases} +\infty & \mathbf{r} = \mathbf{R}^k \\ 0 & \mathbf{r} \neq \mathbf{R}^k \end{cases}. \tag{5}$$

If we denote the continuum points $\mathbf{r}$ in physical space that correspond to discrete atoms $\mathbf{R}^k$ in phase space as $\mathbf{r}_k$, the Dirac δ-function indicates that in mapping phase space into physical space, only the pointwise continuum quantities at $\mathbf{r}_k$ are sampled. The mechanical variables at $\mathbf{r}_k$ are related to the atomic values at $\mathbf{R}^k$ by

$$\rho(\mathbf{r}_k)\ddot{\mathbf{r}}_k = \frac{m^k}{\Omega^k}\ddot{\mathbf{R}}^k \tag{6}$$

$$\mathrm{f}_{\mathrm{int}}(\mathbf{r}_k) = \mathbf{f}_k = \frac{\mathbf{F}^k}{\Omega^k} \tag{7}$$

where Ω^k is the volume of kth atom. At this point, there are many ways to form the continuum field at *any* continuum point. For example, given a set of $\mathbf{r}_k$, Delaunay tessellation can be constructed, where the 3-D physical space is divided into tetrahedra whose vertices are at $\mathbf{r}_k$ (Mott et al., 1992; Stukowski and Arsenlis, 2012). Then, within each 4-atom tetrahedron, for a perfect lattice, the continuum quantities at *any* point can be linearly interpolated from the values at vertices. Line defects (dislocations) and plane defects (e.g., stacking faults and free surfaces) are considered as weak discontinuities, where the interpolation of the mechanical quantities differs. At a free surface, for example, the mechanical quantities should be truncated smoothly in the normal direction. This is because beyond the outer boundaries or within the inner boundaries, most quantities are meaningless. In addition, volume defects such as voids and cracks are considered as strong discontinuities and are excluded from the tessellation. It is beyond the scope of this paper to discuss the details in constructing the tessellation and the discussion below only concerns the continuum quantities at $\mathbf{r}_k$ for brevity.

3. Methods

In the CAC approach, there are atomistic domains and coarse-grained domains with different degrees of coarse-graining, as shown in Fig. 1. The goal of the quasistatic implementation of the CAC approach taken in this paper is to minimize the

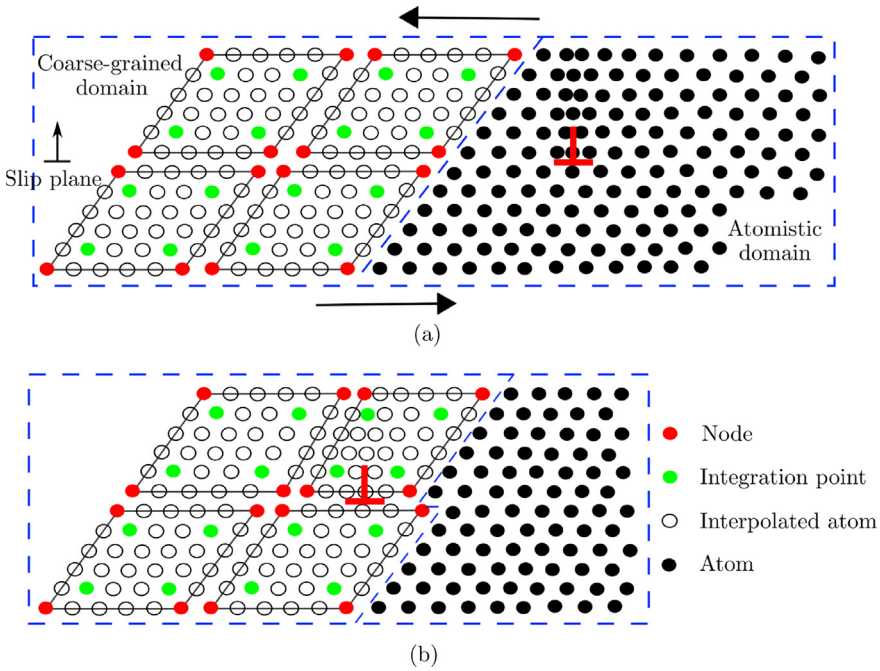

Fig. 1. A 2-D CAC simulation domain consisting of an atomistic domain (right) and a coarse-grained domain (left). The atomistic domain is composed of atoms (black circles), which follow the same governing equations in the atomistic simulation. The coarse-grained domain consists of discontinuous elements of varying size, each of which contains a large number of underlying atoms with the nodes (red circles) as the only degrees of freedom. Only the force/energy on integration points (green circles) and nodes are calculated. The positions of atoms within each element (open circles) are interpolated from the nodal positions. In 3-D, elements have faces on {111} planes, the slip planes of FCC lattice. Note that the elements shown are for illustration purposes only. In (a), an edge dislocation (red ⊥) is located in the atomistic domain. Upon applying a shear stress on the simulation cell, the dislocation migrates into the coarse-grained domain in (b), where the Burgers vector spreads out between discontinuous elements. (For interpretation of the references to colour in this figure legend, the reader is referred to the web version of this article.)

energy of the system for each increment of system loading, which has contributions from both atomistic (e_{at}) and coarse-grained (e_{cg}) domains, i.e.,

$$e_{int}(\mathbf{R}) = e_{at}(\mathbf{R}_{atom}) + e_{cg}(\mathbf{R}_{node}) \tag{8}$$

where e_{int} is the internal energy and $\mathbf{R}$ is the positions of all atoms and nodes, distinguished by associated subscript. The goal is to find $\mathbf{R}$ such that e_{int} is at the minimum when the system is subject to certain boundary conditions. As will be explained later, the atomic force and equivalent nodal force are crucial in the present quasistatic implementation of the CAC approach because they provide information related to the direction along which the atoms/nodes should move during each iteration.

3.1. Atomistic domain

In the atomistic domain, the atomic force $\mathbf{F}^k$ is calculated by the force theorem

$$\mathbf{F}^k = -\nabla_{\mathbf{R}^k} e_{int}. \tag{9}$$

When only fully resolved atomistic domains are considered in the simulation, e_{int} is the summation of well defined atomic energy of all atoms $e_{at}(\mathbf{R}_{atom})$ computed using the interatomic potential, and so the quasistatic CAC method reduces to standard MS.

3.2. Coarse-grained domain

3.2.1. Discretization

To solve Eq. (1) in the coarse-grained domain, it can be daunting to compute the forces on each atom, so a finite element approach is employed. Note that the physical space is continuous in a defect free perfect lattice, and so is the displacement field $\mathbf{u}$. As indicated previously, the displacement discontinuity in the coarse-grained domain is accounted for by interelement discontinuity. Rhombohedral elements with all faces lying on {111} planes are selected for several reasons: (1) slip in FCC metals occurs along close-packed {111} planes, (2) the elements conform to the FCC lattice, (3) the smallest rhombohedral element is a primitive unit cell in the atomistic domain, and (4) a balance between 2-D triangular elements (would be tetrahedral elements if in 3-D) with high efficiency (Deng et al., 2010) and 3-D hybrid elements with high accuracy (Deng and Chen, 2013) that were employed in our earlier work.

Within each element, lattice defects are not allowed and the displacement field has C^1 continuity. Between elements, however, neither displacement continuity nor strain compatibility is required. The lack of such requirements does not preclude description of a perfect lattice over large domains involving many elements, nor does it imply that all types of defects can be captured, particularly at high resolution. Lattice defects are accommodated by discontinuous displacements between elements, potentially including both sliding and separation. Domains with full atomic resolution differ from coarse-grained domains by virtue of their ability to resolve lattice defects, for example dislocation cores, although the net Burgers vector of such defects can be captured in the coarse-grained description. Adaptive refinement of coarse-grained elements can be pursued to promote smooth transition of defect migration from atomistic to coarse-grained domains as necessary.

We discretize $\mathbf{u}$ within each element via the relation

$$\mathbf{u} = \mathbf{\Phi}_\xi(\mathbf{r})\mathbf{u}_\xi \tag{10}$$

where $\mathbf{u}$ is a 1×3 vector, ξ are the nodes, the shape function $\mathbf{\Phi}_\xi$ is a $1 \times N_{npe}$ vector, and $\mathbf{u}_\xi$ is a $N_{npe} \times 3$ matrix where N_{npe} is the number of nodes per element. For each node ξ, Φ_ξ is trilinear, i.e.,

$$\Phi_\xi = \frac{1}{8}(1\pm\chi)(1\pm\eta)(1\pm\zeta) \tag{11}$$

where χ, η, and ζ are natural coordinates. Thus, it can be said that the displacement field is discretized by employing a piecewise continuous shape function.

The equivalent nodal force $\mathcal{F}^\xi$ on node ξ is calculated by

$$\mathcal{F}^\xi = \frac{\sum_\mu \omega_\mu \Phi_{\mu\xi} F^\mu}{\sum_\mu \omega_\mu \Phi_{\mu\xi}} \tag{12}$$

where F^μ is the force on the integration point μ, ω_μ the weight, and $\Phi_{\mu\xi}$ the trilinear shape function. The derivation of Eq. (12) and the details of integration points are given in Appendices A and B, respectively.

3.2.2. Piecewise continuous interpolation function

In energy minimization, the variations of the nodal positions in each iteration change the shape of the element and displace the atoms. In a 3-D element, the "surface atoms" are located in subregions α, β, and γ while the "interior atoms" are in

subregion δ, as shown in Fig. B.23. One way to distinguish the displacements of the two types of atoms is to apply different shape functions and interpolation functions in different subregions. In the present work, however, we employ the same shape function for all atoms within an element, with the subregions having different integration points and weights. Moreover, we assume that the deformation of the kth atom within an element, including the integration points, conforms to that of the element, i.e.,

$$\mathbf{R}^k = \phi_{k\xi}\mathbf{R}^\xi \tag{13}$$

where the first order interpolation function ϕ is the same as the trilinear shape function Φ. In this way, each element domain with interpolation in Eq. (13) contains a hyperelastic defect-free lattice that can only have homogeneous deformation, and the element is isoparametric. Since interelement discontinuity is allowed, this essentially represents a piecewise continuous interpolation function in each element.

For more general crystalline materials, the interpolation function fails to properly describe the internal atomic positions within the unit cells. In the case of higher order shape functions, employing the trilinear interpolation function results in subparametric elements. However, in the present work, only monoatomic pure FCC crystals are considered with a trilinear shape function, so the trilinear interpolation function applies.

3.3. Force calculation

In both atomistic and coarse-grained domains, the force $\mathbf{F}$ on atoms or integration points is calculated using Eq. (9). The EAM formulations for potential energy and force are given by

$$e_{\text{int}} = \frac{1}{2}\sum_i \sum_{\substack{j \\ j\neq i}} V\left(R^{ij}\right) + \sum_i F\left(\overline{\rho}^i\right) \tag{14}$$

$$\mathbf{F}^k = \sum_{\substack{j \\ j\neq k}} \left\{ \frac{\partial V\left(R^{kj}\right)}{\partial R^{kj}} + \left[\frac{\partial F\left(\overline{\rho}^k\right)}{\partial \overline{\rho}^k} + \frac{\partial F\left(\overline{\rho}^j\right)}{\partial \overline{\rho}^j}\right] \frac{\partial \rho\left(R^{kj}\right)}{\partial R^{kj}} \right\} \frac{\mathbf{R}^{kj}}{R^{kj}}. \tag{15}$$

Here, V is the pair potential, F is the embedding potential, $\overline{\rho}$ is the host electron density, $\mathbf{R}^{kj}$ is the vector from atom k to atom j with norm R^{kj}

$$\mathbf{R}^{kj} = \mathbf{R}^j - \mathbf{R}^k \tag{16}$$

$$\overline{\rho}^k = \sum_{k\neq j} \rho^{kj}\left(R^{kj}\right) \tag{17}$$

where ρ is the local electron density between an atomic pair. Equation (9) suggests that the force applied on an atom is the negative variation of the internal energy with respect to its displacement. In the atomistic domain, each atom has independent degree of freedom, so we can fix all atoms but k in calculating $\mathbf{F}^k$.

In the coarse-grained domain, however, when integration points μ and their neighbors j are in the same element, they are bound by the interpolation function, so we can't move μ while fixing j. In this regard, the force that needs to move an atom by the same displacement is slightly larger than that in atomistic domain because of the collective displacements of other atoms given the non-local force field.

3.4. Energy calculation

In the atomistic domain, the internal energy e_{int} is the sum of the energy of all atoms. Since the force vector field is the negative gradient of the internal energy scalar, it becomes zero when the energy scalar is at the minimum, and vice versa.

In the coarse-grained domain, however, explicitly calculating the energy of all atoms is quite cumbersome. A formulation of e_{int} must be constructed to fulfill two requirements. The first one is that for element I, its energy e_I equals that given by Eq. (14), i.e.,

$$e_I = \sum_k^{N_{\text{ape}}} e^k \tag{18}$$

where N_{ape} is the number of atoms per element.

The second requirement is that the global equivalent nodal force vector is zero when e_{int} is at its minimum.

From Eq. (12), we know that the equivalent nodal force is a linear combination of the atomic force on the integration points. This motivates us to construct e_{int} as a linear combination of the atomic energy of the integration points, i.e.,

$$e_{\text{cg}} = \sum_{I}^{N_{\text{ele}}} e_I = \sum_{I}^{N_{\text{ele}}} \sum_{\xi}^{N_{\text{npe}}} \sum_{\mu}^{N_{\text{ipe}}} \omega_\mu \Phi_{\mu\xi} e^\mu \tag{19}$$

where N_{ele} is the number of elements in the system, N_{ipe} is the number of integration points per element, and e^μ is the atomic energy of integration point μ.

Similar to Eq. (B.4), within a subregion, $e^k = e^\mu$ for all atoms k, i.e.,

$$\sum_{k}^{\omega_\mu} e^k = \omega_\mu e^\mu. \tag{20}$$

Therefore, the element energy in Eq. (19) becomes

$$\begin{aligned} e_I &= \sum_{\xi}^{N_{\text{npe}}} \sum_{\mu}^{N_{\text{ipe}}} \omega_\mu \Phi_{\mu\xi} e^\mu = \sum_{\xi}^{N_{\text{npe}}} \sum_{\mu}^{N_{\text{ipe}}} \Phi_{\mu\xi} \sum_{k}^{\omega_\mu} e^k \\ &= \sum_{\mu}^{N_{\text{ipe}}} \sum_{k}^{\omega_\mu} e^k \sum_{\xi}^{N_{\text{npe}}} \Phi_{\mu\xi} = \sum_{\mu}^{N_{\text{ipe}}} \sum_{k}^{\omega_\mu} e^k = \sum_{k}^{N_{\text{ape}}} e^k \end{aligned} \tag{21}$$

and the first requirement is satisfied.

Regarding the second requirement, when e_{cg} is at its minimum, so is the energy of each integration point e^μ, which leads to zero $\mathbf{F}^\mu$ and $\mathcal{F}^\xi$. The second requirement is thus fulfilled. Its converse, however, is *not* necessarily true, because zero $\mathcal{F}^\xi$ could be achieved by a combination of non-zero $\mathbf{F}^\mu$, where e_{cg} is not at its minimum. Nevertheless, experience shows that such exception rarely if ever occurs.

Following the equivalent nodal force and applying the assumptions in dividing one element into subregions as described in Appendix B, we define the equivalent nodal energy of node ξ as

$$\mathcal{E}^\xi = \frac{\sum_{\mu} \omega_\mu \Phi_{\mu\xi} e^\mu}{\sum_{\mu} \omega_\mu \Phi_{\mu\xi}} \tag{22}$$

which is of the same order as the atomic energy.

3.5. Energy minimization

A system at equilibrium corresponds to a local minimum on the potential energy surface. The energy minimization of a many-body system requires that the degrees of freedom are systematically varied until the global minimum is reached. A generic non-linear energy minimization algorithm consists of three steps (Tadmor and Miller, 2012):

1. For each degree of freedom in global position vector **R**, find the global direction vector **d** and the global step size α.
2. Update **R** to $\mathbf{R} + \alpha\mathbf{d}$ to get the minimum of potential energy along **d**.
3. Calculate the new potential energy, update **d**.

Non-linear energy minimization methods differ from each other in that the direction vector **d** is computed in different ways. Steepest descent and conjugate gradient methods are employed in CAC simulations. Both methods use the negative gradient of potential energy as the initial direction; from the second step, however, the steepest descent method uses the current negative gradient while the conjugate gradient method uses the negative gradient conjugated to the current potential surface. Iteration stops when some tolerance criterion is satisfied.

In a CAC simulation, whenever we need the negative gradient vector of potential energy, we adopt the current global force vector $\mathbf{F}_{\text{global}}$, i.e., the atomic force vector is concatenated with the equivalent nodal force vector,

$$\mathbf{F}_{\text{global}} = \begin{bmatrix} F^1_{\text{atom}} \\ \vdots \\ F^{N_{\text{atom}}}_{\text{atom}} \\ 0 \\ \vdots \\ 0 \end{bmatrix} + \begin{bmatrix} 0 \\ \vdots \\ 0 \\ \mathcal{F}^1_{\text{node}} \\ \vdots \\ \mathcal{F}^{N_{\text{node}}}_{\text{node}} \end{bmatrix} \tag{23}$$

where N_{node} is the number of nodes.

Table 1
Quasistatic CAC algorithm. λ is the controlled loading and $\Delta\lambda$ is the loading step size.

Step	Atomistic domain	Coarse-grained domain	Methods
1	Initialize $\mathbf{R}^k(\lambda)$	Initialize $\mathbf{R}^\xi(\lambda)$	
2		Calculate $\mathbf{R}^k(\lambda)$ from $\mathbf{R}^\xi(\lambda)$	Eq. (13)
3	Calculate $\mathbf{F}^k(\lambda)$	Calculate $\mathbf{F}^\mu(\lambda)$	Eq. (15)
4		Calculate $\mathcal{F}^\xi(\lambda)$	Eq. (12)
5	Calculate $\mathbf{d}^k(\lambda)$	Calculate $\mathbf{d}^\xi(\lambda)$	
6	Calculate $\alpha(\lambda)$		line search
7	$\mathbf{R}^k(\lambda) = \mathbf{R}^k(\lambda) + \alpha(\lambda)\mathbf{d}^k(\lambda)$	$\mathbf{R}^\xi(\lambda) = \mathbf{R}^\xi(\lambda) + \alpha(\lambda)\mathbf{d}^\xi(\lambda)$	
8	Calculate $e_{\text{int}}(\mathbf{R})$ if necessary		Eq. (8)
9	Repeat from step 2 until the tolerance is reached		
10	Advance loading step, get $\mathbf{R}(\lambda + \Delta\lambda)$		
11	Repeat from step 2		

In practice, however, the step size α is applied for all degrees of freedom. While this has numerical benefits, a constraint is accordingly applied on the minimization process, such that the energy of each atom can't reach its individual minimum simultaneously. This means that the computed minimum system energy is slightly larger than the exact result. The length of the global force vector is also only *close to* zero when the minimized e_{int} is found, and vice versa. It follows that we have two equivalent tolerance criteria: (1) the energy variation between successive iterations divided by energy from the current step is close to zero and (2) the length of the global force vector is sufficiently small. The second criterion suggests that we could minimize the system energy by directly zeroing the global force vector. Two methods to do this — the quenched dynamics method (Sheppard et al., 2008) and the fast inertial relaxation engine (FIRE) method (Bitzek et al., 2006) — are also included in CAC algorithm, but are not used in the simulations reported in this particular paper. Moreover, the size/shape of the simulation box can be adjusted during the energy minimization to converge to the desired stress tensor (Tadmor and Miller, 2012).

3.6. CAC simulation theme

The CAC simulation scheme is summarized by the recipe in Table 1. In practice, to have a reasonably fast convergence of the energy minimization process, a loading step size $\Delta\lambda$ varying from $0.001a_0$ to $0.01a_0$ is employed, where a_0 is the lattice parameter. The minimization is considered to converge when the absolute energy variation between successive iterations divided by the energy magnitude is smaller than either 10^{-5} or 10^{-6}. Some algorithmic issues in CAC implementation are presented in Appendix C.

4. Discussion

4.1. Non-local nodes

In the QC method, the repatoms are categorized into local and non-local types, according to a *nonlocality* criterion (Tadmor et al., 1996). Local atoms are used when the energy of an element is determined only by its deformation gradient. A large deformation gradient is manifested where the deformation is plastic due to emergent lattice defects, and so the eigenvalue of the deformation gradient can capture the *nonlocality*, which is used to decide if the nodes are local or non-local and if the coarse-grained domains need to be refined.

In CAC simulations, each element is a hyperelastic body that can only have elastic deformation, and the relative displacement (slip) between elements accommodates plastic deformation such as dislocation migration. In QC, in contrast, the deformation is continuous. Thus, the deformation gradient of a single element in CAC is generally smaller than that in QC especially in the presence of plasticity; in other words, the deformation gradient alone can't be used to assess the *nonlocality*. On the other hand, for general formulations all nodes must be non-local, prepared for any possible case. Therefore, all force/energy calculations in CAC simulations, are non-local, i.e., across the atomistic/coarse-grained domain interface, the motion of nodes cause forces on atoms and vice versa. When the interface lies within an infinitely large perfect lattice subject to a homogeneous deformation, the forces on all kth atoms in the atomistic domain and those on all μth integration points in the coarse-grained domain are the same, because the trilinear interpolation function precisely represents the atomic positions under homogeneous deformation, i.e.,

$$\mathbf{F}^k = \mathbf{F}^\mu = \mathbf{F}_{\text{homo}} \tag{24}$$

Substituting Eq. (24) into Eq. (12), it follows that the equivalent nodal force on all ξth nodes are $\mathbf{F}_{\text{homo}}$, i.e., no extra force is introduced compared with an equivalent full atomistic model. Therefore, there is no ghost force at the domain interface in both undeformed and homogeneously deformed configurations.

4.2. Equivalent nodal force/energy

In the coarse-grained domain, the equivalent nodal force $\mathcal{F}^{\xi}$ and energy $\mathcal{E}^{\xi}$ are defined in Eq. (12) and Eq. (22), respectively. While the choice of the integration points have been discussed in Appendix B, one may wonder why we don't simply use the atomic force/energy of the node, i.e.,

$$\mathcal{F}^{\xi} = \mathbf{F}^{\xi} \quad \text{and} \quad \mathcal{E}^{\xi} = e^{\xi}. \tag{25}$$

The equation implies that the nodes are the only integration points. Employing Eq. (B.1), we have

$$\omega_{\xi} = \frac{N_{\text{ape}}}{N_{\text{npe}}} \tag{26}$$

which suggests that one node represents a group of ω_{ξ} number of atoms. This choice of integration points overestimates the force/energy if the nodes don't reside in a perfect lattice. For example, when a node is at a corner in the vicinity of three free surfaces, its force is larger than the atomic force of an atom inside a perfect lattice. Equation (26) means that the group of ω_{ξ} number of atoms represented by the node identically has the same environment (i.e., at the corner), which will unavoidably lead to the overestimation of the force. In practice, adopting Eq. (25) results in large displacement of the nodes on the traction free boundary within a few simulation steps.

A similar instability of the nodal integration scheme occurs in the meshfree particle method. Beissel and Belytschko (1996) found that although the nodal integration of a Galerkin approximation is faster and easier to implement than the quadrature method, it results in a spatial instability. One approach to stabilize the integration is to use additional quadrature points (Dyka et al., 1997). Later, Xiao and Belytschko (2005) and Rabczuk et al. (2004) concluded that while the interpolation in Eulerian coordinate affects material instability, an interpolation in Lagrangian coordinates promotes numerical stability. In CAC simulations, such interpolation is realized by the application of a piecewise continuous interpolation function within elements, which is essentially of Lagrangian type although the balance laws are expressed in Eulerian coordinates.

4.3. Quasistatic stress calculation

In CAC, the 2nd rank Cauchy stress tensor $\boldsymbol{\sigma}$ is calculated *a posteriori*. In the atomistic domain, the average stress of a region with volume Ω_{at} is given by

$$\boldsymbol{\sigma}_{\text{at}} = \frac{1}{2\Omega_{\text{at}}} \sum_{k} \sum_{\substack{j \\ j \neq k}} \mathbf{R}^{kj} \otimes \mathbf{F}^{kj}. \tag{27}$$

In the coarse-grained domain, the average stress of a region with volume Ω_{cg} is given by

$$\boldsymbol{\sigma}_{\text{cg}} = \frac{1}{2\Omega_{\text{cg}}} \sum_{I}^{N_{\text{ele}}} \sum_{\mu} \omega_{\mu} \boldsymbol{\Phi}_{\mu\xi} \sum_{\substack{j \\ j \neq \mu}} \mathbf{R}^{\mu j} \otimes \mathbf{F}^{\mu j}. \tag{28}$$

So in a CAC simulation cell, the average stress is

$$\boldsymbol{\sigma}_{\text{sys}} = \frac{\boldsymbol{\sigma}_{\text{at}}\Omega_{\text{at}} + \boldsymbol{\sigma}_{\text{cg}}\Omega_{\text{cg}}}{\Omega_{\text{at}} + \Omega_{\text{cg}}}. \tag{29}$$

The atomic stress at atom k with volume Ω^{k} is defined as

$$\boldsymbol{\sigma}^{k} = \frac{1}{\Omega^{k}} \sum_{\substack{j \\ j \neq k}} \mathbf{R}^{kj} \otimes \mathbf{F}^{kj}. \tag{30}$$

The equivalent nodal stress at node ξ

$$\mathcal{S}^{\xi} = \frac{\sum_{\mu} \omega_{\mu} \boldsymbol{\Phi}_{\mu\xi} \boldsymbol{\sigma}^{\mu}}{\sum_{\mu} \omega_{\mu} \boldsymbol{\Phi}_{\mu\xi}} \tag{31}$$

which is of the same order as the atomic stress.

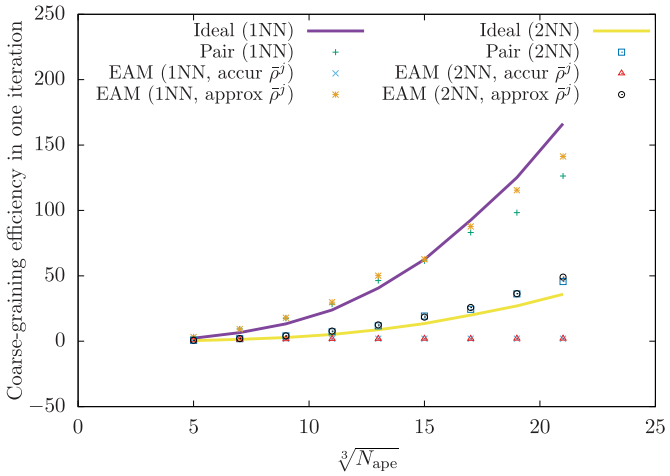

Fig. 2. Coarse-graining efficiency of CAC simulations as a function of element size. Time for both force/energy calculation and neighbor list updating is included. Both employing EAM potentials, EAM (accur $\bar{\rho}^j$) calculates the host electron density $\bar{\rho}$ of all atoms, while EAM (approx $\bar{\rho}^j$) only calculates $\bar{\rho}$ of the integration points and it is assumed that all atoms in the same subregion within one element have the same $\bar{\rho}$ as that of the integration point. It is found that both pair and EAM potentials (with proper approximation) give coarse-graining efficiency of 150 for 1NN element and 50 for 2NN element when $N_{\text{ape}} = 9261$.

4.4. Coarse-graining efficiency in one iteration

In estimating the ideal coarse-graining efficiency in one iteration, ψ_{cg}, we assume that each atom or integration point has N_{nei} number of neighbors within the cutoff distance; then, in one element in the coarse-grained domain, there are $N_{\text{ipe}}N_{\text{nei}}$ unique atomic pairs. In the equivalent atomistic domain, there are $N_{\text{ape}}N_{\text{nei}}/2$ unique atomic pairs. This suggests that $\psi_{\text{cg}} = N_{\text{ape}}/(2N_{\text{ipe}})$. If $N_{\text{ape}} = 2197$, $\psi_{\text{cg}} = 40.69$ for 1NN element and $\psi_{\text{cg}} = 8.79$ for 2NN element. Moreover, ψ_{cg} increases with the element size, as shown in Fig. 2.

The ideal ψ_{cg} is calculated based on the assumption that only the pairs between the integration points and their neighbors are taken into account. Thus, it agrees well with the actual efficiency using a pair potential. In calculating the force on one integration point μ using EAM potential, however, one needs to know the host electron density of its neighbors j (i.e., $\bar{\rho}^j$ in Eq. (15)), which requires considering pairs between j and j's neighbors. The direct calculation of all these pairs includes a significant number of repeated computations because the atoms involved are located in close proximity.

One way to avoid the duplication is to calculate $\bar{\rho}$ of all slave atoms using Newton's third law. While giving accurate $\bar{\rho}$ of the integration points μ and their neighbors j, this method also calculates $\bar{\rho}$ of a large number of unused slave atoms, especially so in a large element with sparse integration points. It is shown that this method gives a low ψ_{cg} around 2.5 for $N_{\text{ape}} = 2197$. Therefore, we introduce a similar approximation as in the force/energy calculation that within one element, $\bar{\rho}$ of the slave

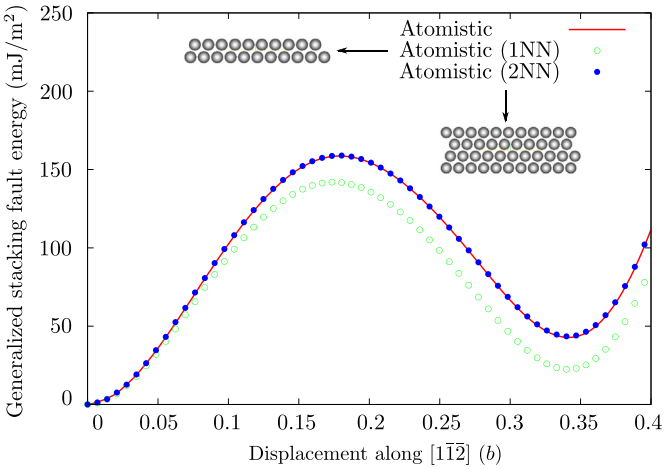

Fig. 3. Relaxed generalized stacking fault energy on $(\mathbf{1\bar{1}1})$ plane along $[\mathbf{1\bar{1}\bar{2}}]$ direction in Cu in a fully atomistic domain. b is the magnitude of Burgers vector $\mathbf{b} = \mathbf{1/2}[\mathbf{1\bar{1}\bar{2}}]\boldsymbol{a_0}$. Consideration of only 2 layers of atoms on each side of the stacking fault is sufficient to reproduce results of full atomistics.

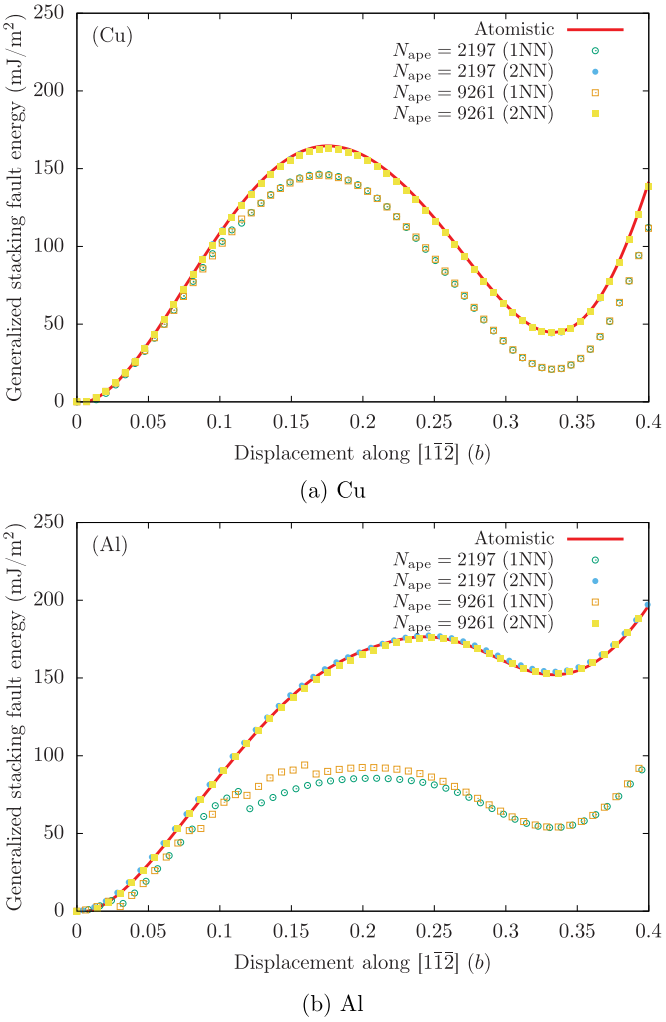

Fig. 4. Relaxed generalized stacking fault energy on $(\mathbf{1\bar{1}1})$ plane along $[\mathbf{1\bar{1}\bar{2}}]$ direction in both Cu and Al in the coarse-grained domain. b is the magnitude of Burgers vector $\mathbf{b} = \mathbf{1/2}\,[\mathbf{1\bar{1}\bar{2}}]\boldsymbol{a_0}$. The 2NN element provides more accurate predictions than the 1NN element.

atoms in one subregion equals that of the integration points in the same subregion (see Fig. B.26 for the illustration of subregion). In this way, we need only to calculate $\overline{\rho}$ of the integration points, and the coarse-graining efficiency is increased substantially, which is shown as EAM (approx $\overline{\rho}^j$) in Fig. 2. It is found that if $N_{ape} = 9261$, $\psi_{cg} \approx 150$ for 1NN element and $\psi_{cg} \approx 50$ for 2NN element. Note that in parallel computing, a similar method as in Appendix C is needed to estimate $\overline{\rho}$ in the elements shared by multiple processors.

The coarse-graining efficiency shown in Fig. 2 is calculated by comparing the number of arithmetic operations required in both domains in one iteration. Hence, ψ_{cg} is also the efficiency of dynamic CAC. The quasistatic approach, however, involves an outer iteration loop which sets the search direction and an inner iteration loop in which a line search algorithm is performed, while ψ_{cg} is only the efficiency within one iteration. In the conjugate gradient method, e.g., the outer iteration converges in at most n steps where n is the number of degrees of freedom in system. This suggests that the energy minimized structure may be more rapidly achieved in the coarse-grained domain than in the atomistic domain. The coarse-graining efficiency of the energy minimization method will be explored in Section 5.2.

5. Applications and validation

We next apply quasistatic CAC applications to certain benchmark problems, including generalized stacking fault energy, core structure and stress field of a single 60° mixed type dislocation, surface indentation, and 60° mixed type dislocation migration between atomistic and coarse-grained domains. We choose 60° mixed type dislocation because it has both edge and screw components and is more general. All simulations – fully atomistic, fully coarse-grained, CAC – are quasistatic (0 K).

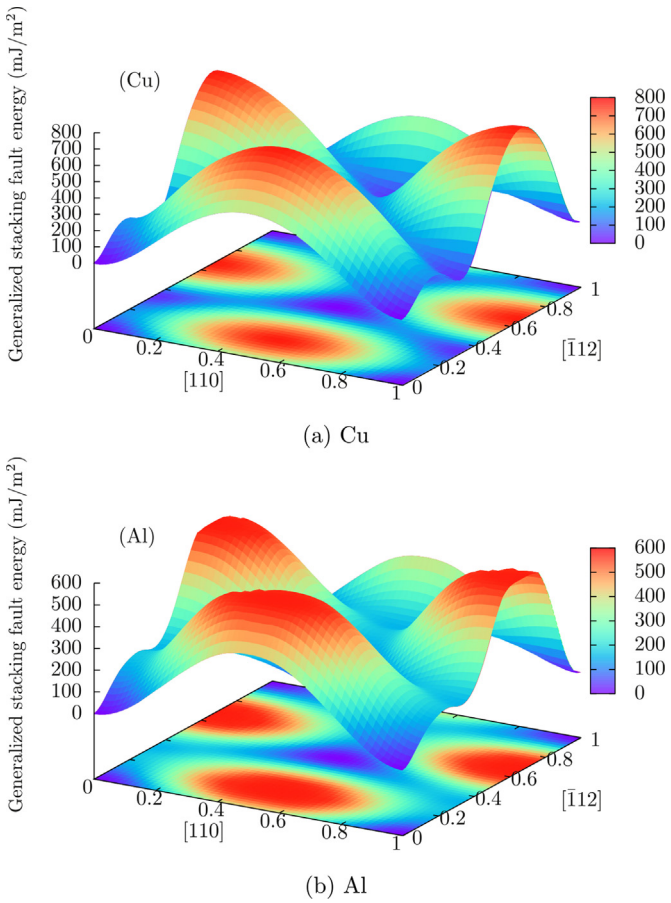

Fig. 5. Relaxed generalized stacking fault energy surface on ($1\bar{1}1$) plane along both [$11\bar{2}$] and [110] directions in both Cu and Al in the coarse-grained domain. The energy surface is close to the results given in the full atomistics, with relative error less than 5%.

All models are fully 3-D with periodic boundary conditions (PBCs) applied along the dislocation line direction. Models for both Cu and Al are of the same size except for a different lattice parameter. EAM potentials for Cu (Mishin et al., 2001) and Al (Mishin et al., 1999) are employed because they well reproduce the generalized stacking fault energy curve as predicted by experiments (Chassagne et al., 2011). In the coarse-grained domain, 2NN elements with $N_{\text{ape}} = 2197$ are employed unless indicated otherwise. The calculations involving the atomic structures, including disregistry, von Mises shear invariant, and Burgers vector, are performed after the atomic positions are interpolated from the nodal positions. We apply the approximation that within one element all atoms in one subregion have the same host electron density. Energy minimization is achieved using the conjugate gradient method after each deformation increment step. In each case, multiple loading step sizes are evaluated such that the results are step size independent. The minimization is considered to converge when the absolute energy variation between successive iterations divided by the energy magnitude is smaller than 10^{-6}. Simulation results are visualized using ParaView (Schroeder et al., 2006) and OVITO (Stukowski, 2010). A preliminary convergence and error analysis based on the results is presented.

5.1. Generalized stacking fault energy

Both the stable and unstable stacking fault energies on {111} planes along ⟨112⟩ directions are relevant in modeling dislocation nucleation and migration in FCC metals (Van Swygenhoven et al., 2004). In the atomistic domain, the generalized stacking fault energy (GSFE) is calculated as

$$e_{\text{SF}} = \frac{e_{\text{at}} - e_{\text{coh}} N_{\text{at}}}{A_0} \tag{32}$$

where e_{at} and N_{at} are the total energy and number of atoms, respectively, e_{coh} is the cohesive energy per atom, and A_0 is the faulted area. The atoms considered are usually up to 8 to 10 layers on each side of the stacking fault. Fig. 3 shows that

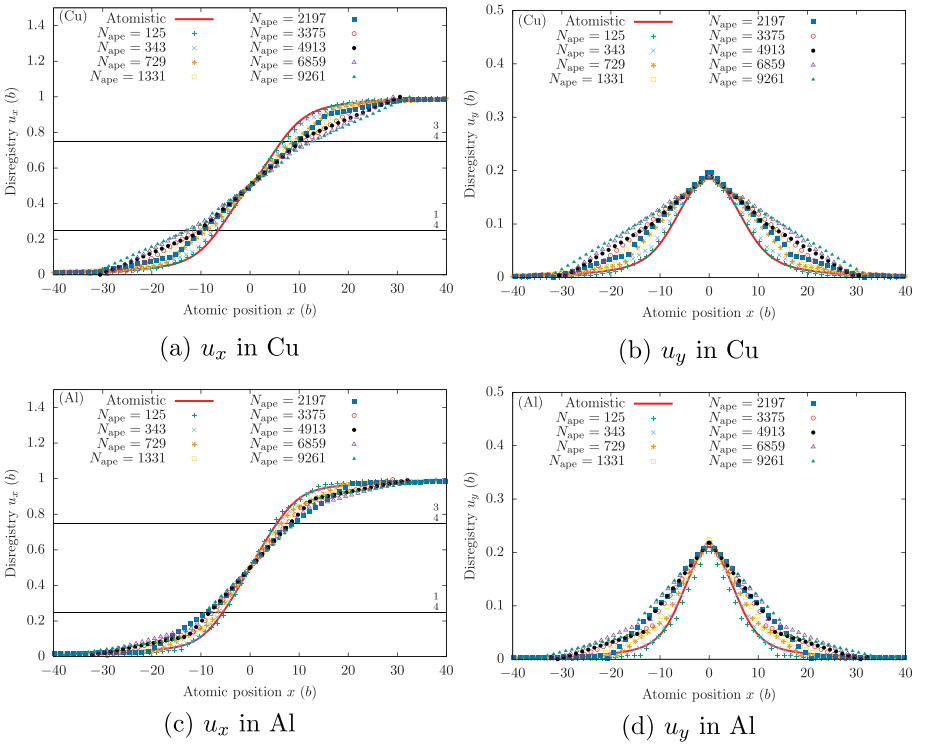

Fig. 6. The disregistry u_x and u_y are the displacements of the dislocation core atoms from their perfect crystal positions parallel to and normal to Burgers vector $\mathbf{b} = \mathbf{1/2}\,\boldsymbol{a_0}[\bar{\mathbf{1}}\mathbf{01}]$, respectively. The results in the coarse-grained domain with varying element size N_{ape} from 125 to 9261 are compared with those of the atomistic domain in both Cu and Al. The disregistry is $b/2$ at the center of the dislocation. In the coarse-grained domain, there is a linear correlation between disregistry and atomic position within an element, due to the trilinear interpolation function.

considering only 2 layers of atoms on each side is sufficient to calculate the generalized stacking fault energy on $(1\bar{1}1)$ plane along $[1\bar{1}\bar{2}]$ direction in Cu. This is also true for Al, though the results are not given here.

In the coarse-grained domain, the 1NN and 2NN elements consider only the force/energy up to 1 and 2 layers of atoms on each side, respectively, of the interface. In calculating the stacking fault energy, e_{at} and N_{at} in Eq. (32) are replaced by e_{cg} and N_{cg}, respectively. Fig. 4 shows that the 2NN element gives more accurate results in both Cu and Al compared to fully resolved atomistic than the 1NN element, regardless of the element size. Both stable and unstable stacking fault energy (γ_{sf} and γ_{usf}) as well as their ratio γ_{sf}/γ_{usf} provided by 1NN element are lower than that of the atomistic domain. As suggested by Van Swygenhoven et al. (2004), a lower γ_{sf}/γ_{usf} ratio is companied by a higher energy barrier to nucleate the trailing partial dislocation. This finding explains the previous observation using 1NN elements that the amplitudes of strain bursts in the stress–strain curves after yielding are larger in the coarse-grained domain than the atomistic domain (Xiong et al., 2012a).

The study is then extended to the generalized stacking fault energy surface that is on $(1\bar{1}1)$ plane along both $[1\bar{1}\bar{2}]$ and $[110]$ directions. The energy surface obtained in the coarse-grained domain (Fig. 5) is close to that of the fully atomistics, with relative error less than 5%.

As discussed in Appendix B, the newly developed 2NN elements better capture dislocation-mediated surface rearrangement/reconstruction, leading to improved characterization of the generalized stacking fault energy. To our knowledge, no other coarse-grained atomistic approaches in the literature are able to accurately describe dislocation core level effects in the coarse-grained domain without fully atomistic mesh refinement.

5.2. Core structure and stress field of a single 60° mixed type dislocation

In FCC metals, a perfect dislocation is dissociated into an extended one that consists of two partial dislocations separated by a stacking fault. In describing the reactions between dislocations and lattice defects, it is important to obtain a correct dislocation core structure. We explore the core structure and stress field of a single 60° mixed type dislocation with Burgers vector $\mathbf{b} = (1/2)a_0[\bar{1}01]$ in the coarse-grained domains in both Cu and Al with element size N_{ape} varying from 125 to 9261. The dislocation is created by displacing a part of the model along $[\bar{1}01]$ direction on $(1\bar{1}1)$ plane. The total displacement, $(\sqrt{2}/2)a_0$, is reached in 180 simulations steps with $0.004a_0$ each step.

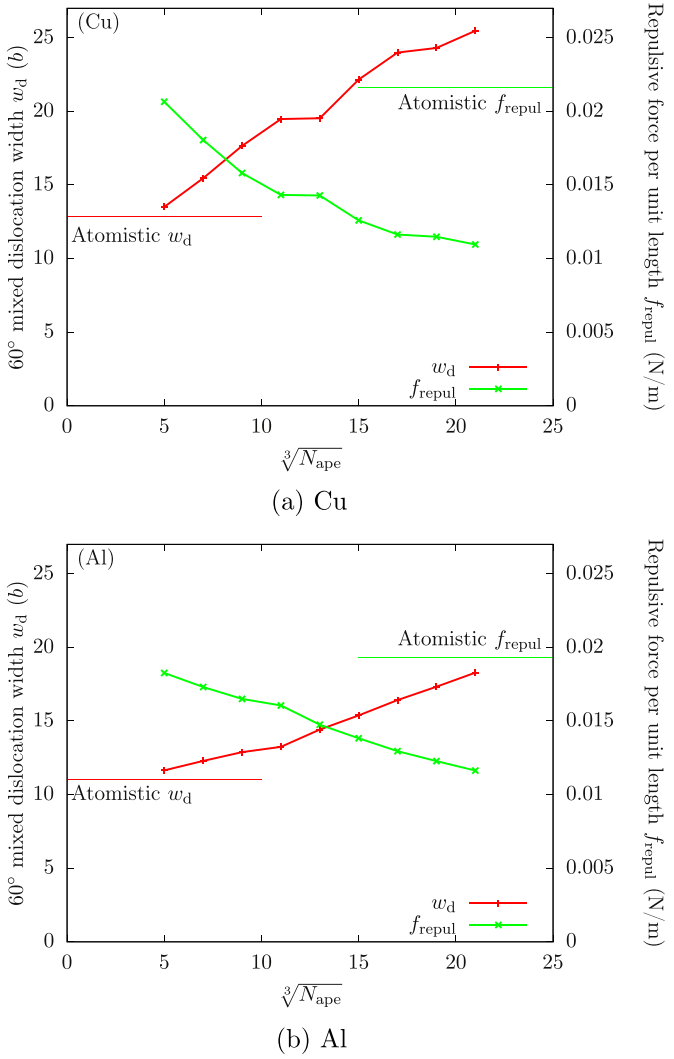

Fig. 7. In both Cu and Al, the coarse-grained domain gives a larger dislocation width than the atomistic domain, and w_d increases with element size. As a result, the repulsive force per unit length between two partial dislocations, f_{repul}, decreases with element size. f_{repul} is calculated using Eq. (33). For Cu, $G = 41.17$ GPa and $b_p = 1.4758$Å; for Al, $G = 28$ GPa and $b_p = 1.6534$Å.

Disregistry, which is the displacement of dislocation core atoms from their perfect crystal positions, is employed to represent the core structure, as shown in Fig. 6; u_x and u_y are the disregistry parallel to and normal to the Burgers vector, respectively. It is found that in the coarse-grained domain, there is a linear correlation between disregistry and atomic position within an element, due to the trilinear interpolation function. Thus, as the element size increases, the coarse-grained domain gives a "flatter" dislocation core structure, which agrees with the larger distance between two partial dislocations. It is therefore advisable to employ a smaller element (e.g., $N_{ape} = 125$) to better capture the dislocation core structure in the coarse-grained domain.

The width of the 60° mixed type dislocation w_d is defined as the distance over which the disregistry parallel to the Burgers vector is greater than 1/4 of the magnitude of the Burgers vector. w_d is also the stable stacking fault width in energy minimization. It is shown that in both Cu and Al, the coarse-grained domain gives a larger dislocation width than the atomistic domain, and w_d increases with element size N_{ape} (Fig. 7). Because the dislocation dissociation is energetically favorable (Frank's rule), a repulsive force per unit length f_{repul} exits between leading and trailing partial dislocations (Hull and Bacon, 2011). Assume that the Poisson's ratio is zero, for any dislocation line orientations, we may write

$$f_{repul} = \frac{Gb_p^2}{4\pi w_d} \tag{33}$$

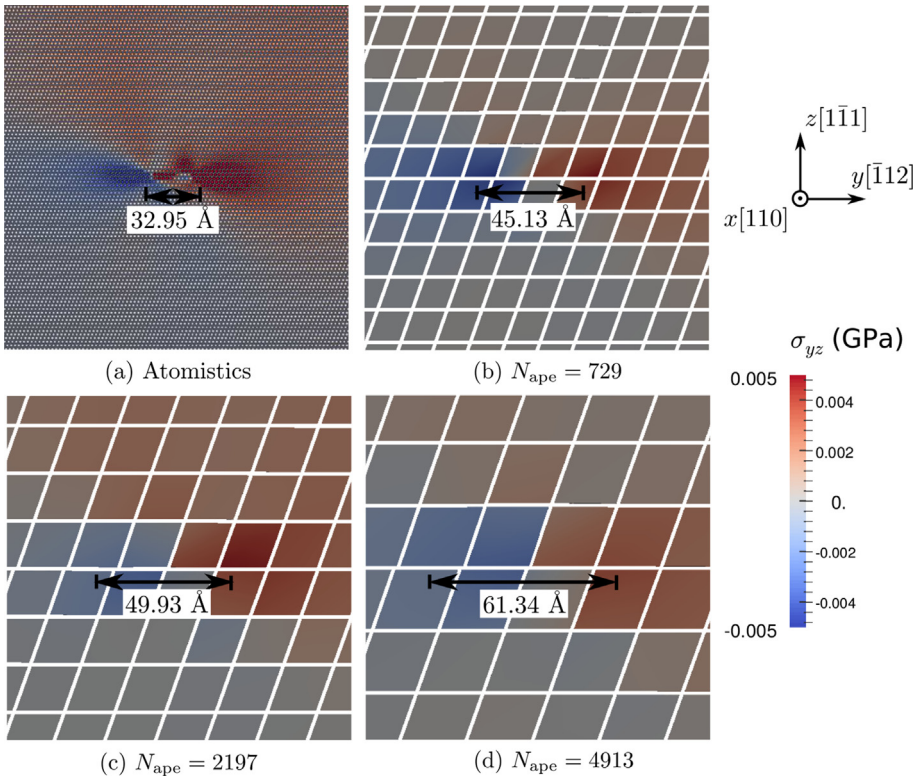

Fig. 8. Snapshots of the shear stress field around a single 60° mixed type dislocation in both atomistic and coarse-grained domains in Cu. A higher degree of coarse-graining gives a wider dislocation core width, as well as a reduced maximum magnitude of shear stress. In the coarse-grained domain, the far field stress away from the dislocation core is preserved. Note that σ_{yz} is for the edge component only since it is zero for the screw component.

where G is the shear modulus and b_p is the magnitude of Burgers vector of the partial dislocations. Consequently, f_{repul} in the coarse-grained domain is smaller than that in the atomistic domain, and the larger the element, the smaller the f_{repul}. Besides the repulsive force, there is also an attractive force per unit length f_{attra} acting to bring the partials together: the coarse-grained domain gives accurate f_{attra} because the latter is provided by the stable stacking fault energy.

In the atomistic domain, f_{attra} balances f_{repul}. In the coarse-grained domain, however, the difference between f_{attra} and f_{repul} must be compensated by an extra force caused by the constraint of the atomic position imposed by the trilinear interpolation function, i.e.,

$$f_{\text{attra}} = f_{\text{repul}} + f_{\text{constr}} \tag{34}$$

where f_{constr} increases with element size.

Our simulations show that the dissociation of a 60° mixed type dislocation into partials is affected by the degree of coarse graining in view of the altered packing sequence in the stacking fault. In addition, the maximum magnitude of shear stress at dislocation core decreases with an increasing element size, while the far field stress away from the core is preserved, as shown in Fig. 8.

These imply that although dislocations migrate within the coarse-grained domain with reasonable approximation as well as correct overall long range stress and Burgers vector, the core structures and dislocation interactions are better described in the atomistic domain, an intuitive result. In addition, elements with graded sizes should be applied in a way that smaller elements are used in the vicinity of the atomistic domain (where dislocation nucleation and primary interactions occur) while larger elements are adopted to address long range fields of arrays of dislocations. Although it was shown earlier using Lennard-Jones (LJ) potential that dislocation–dislocation interactions are reasonably well replicated in the coarse-grained domain (Xiong et al., 2012a), the results with EAM potentials remain to be studied in detail.

As discussed in Section 4.4, the coarse-graining efficiency in quasistatic CAC is more complicated than that of the dynamic CAC method. In the coarse-grained domain, (1) the efficiency in one iteration is higher because only force/energy on integration points are calculated; (2) in theory, the outer iteration loop (i.e., determining the search direction) converges faster because of reduced number of degrees of freedom; (3) the inner loop (i.e., line search algorithm to find the global step size) takes the same number of iterations as for the atomistic domain because the magnitude of direction vector for one node (i.e., equivalent nodal force) is of the same order as that for one atom. It is therefore expected that while the coarse-graining

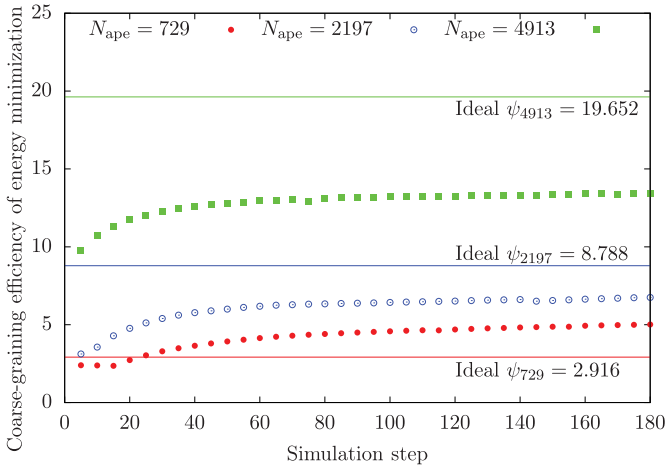

(a) Periodic boundary

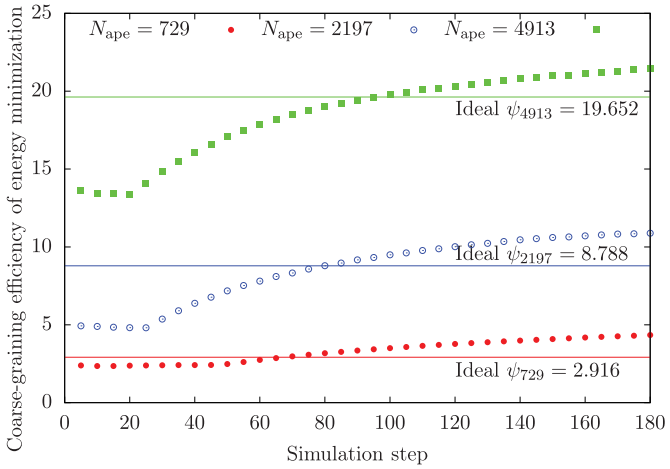

(b) Non-periodic boundary

Fig. 9. Coarse-graining efficiency of energy minimizing a single 60° mixed type dislocation in a model (a) with PBCs and (b) without PBCs along dislocation line direction. It is found that while filling in the periodic boundary with atoms reduces the efficiency, the quasistatic approach achieves a higher coarse-graining efficiency relative to the dynamic method because the outer iteration loop converges faster. The runs were completed using Blacklight on Extreme Science and Engineering Discovery Environment (XSEDE) (Towns et al., 2014).

efficiency of energy minimization should be higher than that of the dynamic CAC method, it is limited by the line search algorithm, whose convergence rate varies from case to case.

The coarse-graining efficiency of energy minimizing a single dislocation is calculated at each simulation step by $\psi = t_{at}/t_{cg}$, where t is the runtime for each case, as shown in Fig. 9a. It is found that: (1) compared with the last 150 simulation steps, ψ of the first 30 steps is lower due to the low efficiency in energy minimizing stress free surfaces (which occurs in the first 30 steps), and (2) larger elements give higher ψ. However, expect for the smallest element ($N_{ape} = 729$), ψ is lower than the ideal full coarse-graining efficiency in one iteration. This is attributed to the atoms that fill in the periodic boundary along the dislocation line direction — a model with larger elements requires a larger number of atoms to fill in at the boundary.

Therefore, we also investigate ψ of energy minimizing the same dislocation in fully coarse-grained models with non-PBC along the dislocation line direction, as shown in Fig. 9b. The lower efficiency at the initial stage lasts about 80 simulation steps because more stress free surfaces need to be relaxed. After that, ψ becomes higher than the ideal efficiency in one iteration because the outer iteration loop converges faster.

5.3. Indentation at a surface

Materials with a high surface-area-to-volume ratio have mechanical properties that differ from bulk materials (Zhu et al., 2008). For example, the hardness of a nano-thin film is known to be a function of the film thickness, and the relevant nano-

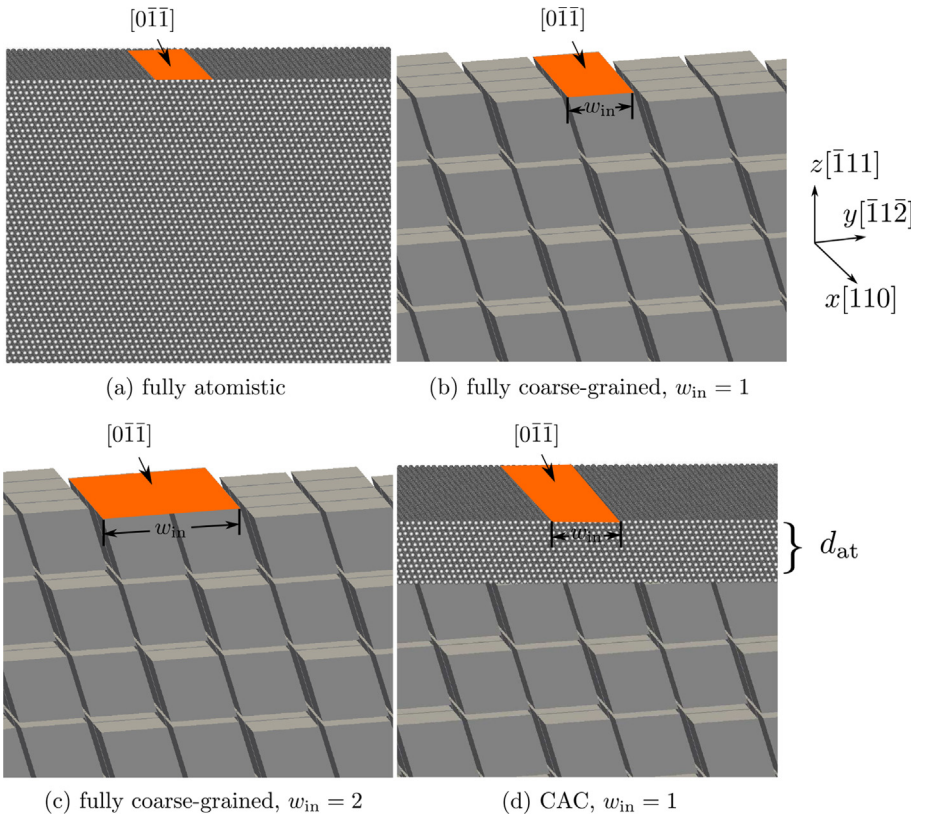

Fig. 10. Simulation cell of surface indentation by (a) fully atomistic, (b) and (c) fully coarse-grained with different indenter width, and (d) CAC simulations with the atomistic domain at the free surface. PBCs are applied along both x and y directions. To apply the periodic boundaries in the coarse-grained domain, the jagged interstices are filled in with atoms, which are not shown here. A plane indenter is applied along $[\mathbf{0\bar{1}\bar{1}}]$ direction by $0.001a_0$ each step in Cu, while the bottom layers of atoms/nodes are fixed. In (d), different d_{at} are employed to quantify the free surface deformation.

indentation process has been widely studied by atomistic simulations. In coarse-graining, however, the lattice deformation at a free surface may not be accurately captured due to its localized nature (Park and Im, 2008): the trilinear interpolation function poses a restriction on the atomic configuration, particularly when a large element is employed. Moreover, the assumption that all atoms in a subregion have the same force/energy is only valid when the deformation gradient within an element remains nearly the same, which is not the case for highly inhomogeneous deformation. Therefore, it is necessary to quantify the ability of the coarse-grained domain in describing nano-indentation, shedding light on the treatment of free surfaces in CAC.

We first perform fully atomistic and fully coarse-grained simulations to analyze the nano-indentation on a thin film in both Cu and Al, as shown in Fig. 10. PBCs are applied along both x and y directions, while the z direction is non-periodic. A plane indenter is applied along $[0\bar{1}\bar{1}]$ direction by $0.001a_0$ each step, while the bottom layers of atoms/nodes are fixed. To eliminate the effects of all boundaries but the free surface, sufficiently large models are employed. In Cu, all models have the same size of 184.05 Å × 230.23 Å × 181.58 Å. Simulations in Fig. 10b and c use the same model but different indenter width w_{in}: along y direction the indenter spans over either 1 or 2 elements. Element sizes N_{ape} of 343 and 2197 are employed independently. During the indentation, the force on the indenter along z direction is calculated then divided by the indentation area.

The indentation force–depth curves are plotted in Fig. 11. Compared with the fully atomistic model, the fully coarse-grained model gives a lower and non-monotonically increasing force in the elastic stage, a phenomenon more pronounced with larger element size or indenter spanning. This was not observed in the stress–strain curve of a LJ potential Cu sample subject to uniaxial tension where the dislocations were also nucleated from the free surface of the coarse-grained domain (Xiong et al., 2011). This is perhaps due to the fact that the stress is a quantity averaged over the system while the indentation force here is calculated locally. To further explore the phenomenon, we calculate the von Mises local shear invariant of each atom, following the formulation in work of Shimizu et al. (2007), i.e.,

$$\eta^{\text{Mises}} = \sqrt{E_{12}^2 + E_{13}^2 + E_{23}^2 + \frac{(E_{11} - E_{33})^2 + (E_{22} - E_{33})^2 + (E_{11} - E_{22})^2}{6}} \tag{35}$$

where E_{ij} are the components of the Green–Lagrange strain tensor $\mathbf{E}$, which is calculated by

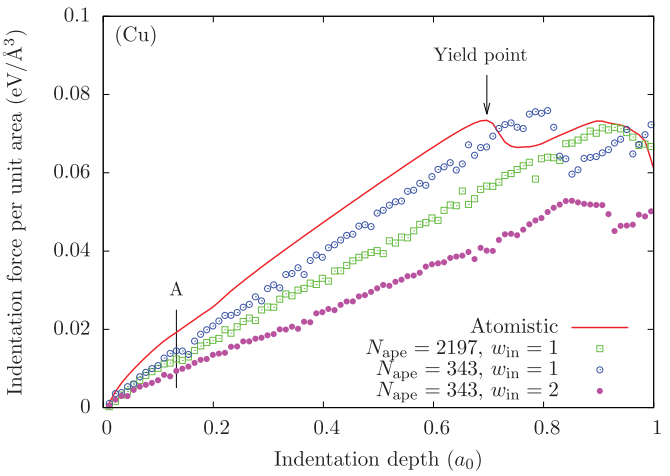

(a) Cu

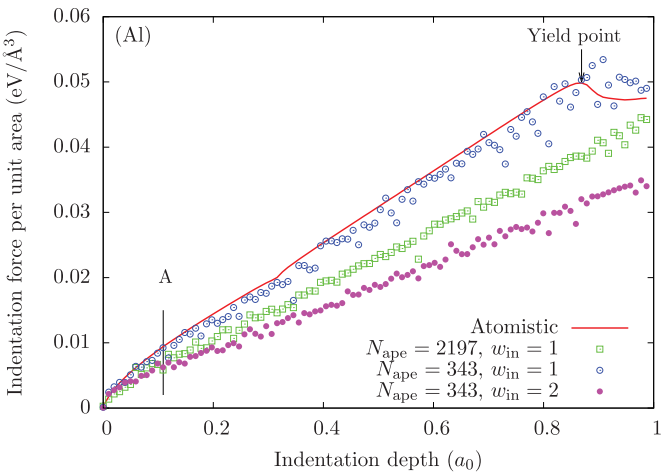

(b) Al

Fig. 11. Indentation force–depth curves obtained from the fully atomistic and fully coarse-grained simulations in both Cu and Al, as shown in Fig. 10a–c. In the fully coarse-grained simulations, element sizes N_{ape} of 343 or 2197 are employed, with the indenter spanning over 1 or 2 element along y direction. Compared with the full atomistics, the fully coarse-grained model gives a lower and non-monotonically increasing force in the elastic stage. In addition, the deviation is larger with larger element or wider indenter.

$$\mathbf{E} = \frac{1}{2}\left(\mathbf{F}^{\top}\mathbf{F} - \mathbf{I}\right) \tag{36}$$

where $\mathbf{I}$ is the 2nd rank identity tensor and $\mathbf{F}$ is the deformation gradient considering only the nearest neighbor interactions in the initial undeformed configuration (Zimmerman et al., 2009). The calculation of η^{Mises} is done by OVITO.

Snapshots of simulations in Cu with atoms colored by η^{Mises} are given in Fig. 12. The indentation depth is $0.144a_0$, corresponding to point A in Fig. 11a. It is found that in the coarse-grained domain, the shear deformation is localized between elements, a phenomenon more pronounced with larger element size. This is due to the trilinear interpolation function employed within the element. In other words, the elastic shear deformation in the coarse-grained domain is confined to a smaller zone than that in the atomistic domain, so a smaller force is sufficient to cause the lattice deformation accommodating the same indentation depth. It is also found that the larger the indenter, the smaller the force per unit area, which agrees with the MS simulations (Tsuru and Shibutani, 2006). Similar phenomena are also found in Al.

The results suggest that when a surface is subject to indentation, the local lattice deformation is not as well reproduced in the coarse-grained domain as in the atomistic domain. Therefore, it is advisable to not apply the indentation directly on a coarse-graining free surface. Instead, fully resolved atomistics should be employed in the vicinity of the indenter when the local elastic deformation gradients are significant. To quantify the required atomistic domain, we perform a series of CAC

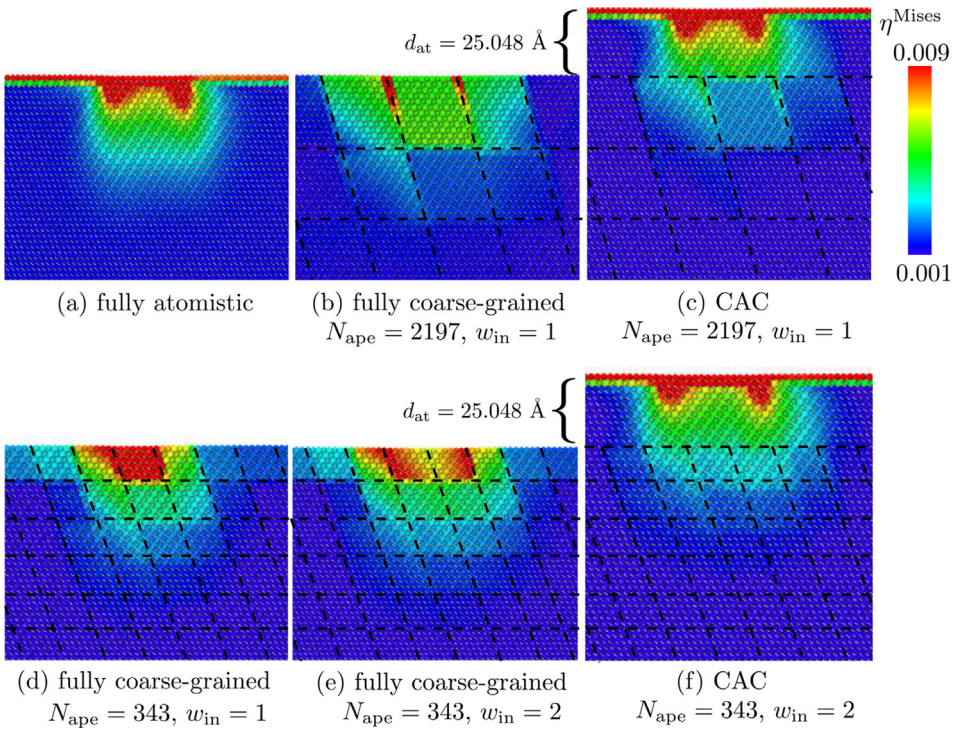

Fig. 12. Snapshots of surface indentation in fully atomistic, fully coarse-grained, and CAC simulations in Cu. The indentation depth is $0.144a_0$, corresponding to point A in Fig. 11a. Atoms are colored by von Mises local shear invariant η^{Mises} (Eq. (35)). In the coarse-grained domain, element sizes N_{ape} of 343 or 2197 are employed and the indenter spans over either 1 or 2 elements. It is shown that the shear deformation is localized between the elements, a phenomenon more pronounced with larger element size or wider indenter. (For interpretation of the references to colour in this figure legend, the reader is referred to the web version of this article.)

simulations, as shown in Fig. 10d. Atomistic domains with different thickness d_{at} are employed at the surface where the indentation is applied.

The indentation force–depth curves show that the larger the d_{at}, the closer the CAC simulation results are to those of the full atomistics. While the shear invariant distribution in the atomistic domain is the same as that in the fully atomistic model, it is disturbed by the atomistic/coarse-grained domain interface and localized between the elements in the coarse-grained domain, as shown in both Fig. 12c and f. The effect of the coarse-graining decreases with increasing d_{at}. We define the optimal atomistic domain thickness as the smallest d_{at} that results in a monotonically increasing force prior to the yield point. The optimal d_{at} values are $13.856a_0$ in Cu and $20.784a_0$ in Al, regardless of the degree of coarse-graining in the model. Thus, we conclude that the optimal d_{at} depends on the material, but not the underlying coarse-grained domain.

5.4. 60° mixed type dislocation migration through the interface between atomistic and coarse-grained domains

One major advantage of CAC compared to the other partitioned domain methods is that dislocations can pass between atomistic and coarse-grained domains without heuristic rules or special provisions. When the slip planes are aligned with the planes between elements, the dislocations pass the domain interface smoothly instead of being reflected or pinned. However, Section 5.2 reveals that the 60° mixed type dislocation has different width in atomistic and coarse-grained domains. This raises the question of how the dislocation width varies as the dislocation migrates across the interface between the two domains and whether this interface affects the dislocation migration significantly. Thus, four cases are considered to clarify distinctions of dislocation migration in fully atomistic, fully coarse-grained, and CAC models in both Cu and Al. All models have the same overall size of 114.55 Å × 173.61 Å × 224.47 Å in Cu. The indentation process and the force calculation are the same as in Section 5.3, except that the indenter moves $0.01a_0$ each step. To eliminate the free surface effect, we fix the top layers (free surface) except those below the indenter, as well as the bottom layers. The fixed atoms/nodes are labeled by red boxes in Fig. 14.

No significant change of indentation force is observed when the dislocation migrates across the interface between atomistic and coarse-grained domain, as shown in Fig. 15. Using the method in Section 5.2, we study the structure of a 60° mixed type dislocation core across the domain interface, as shown in Fig. 16. It is shown that the interface only slightly alters the atomic positions in its vicinity, and the dislocation has a correct core structure once it migrates into the atomistic domain. These results indicate that the domain interface only slightly affects the dislocation migration process in quasistatic CAC.

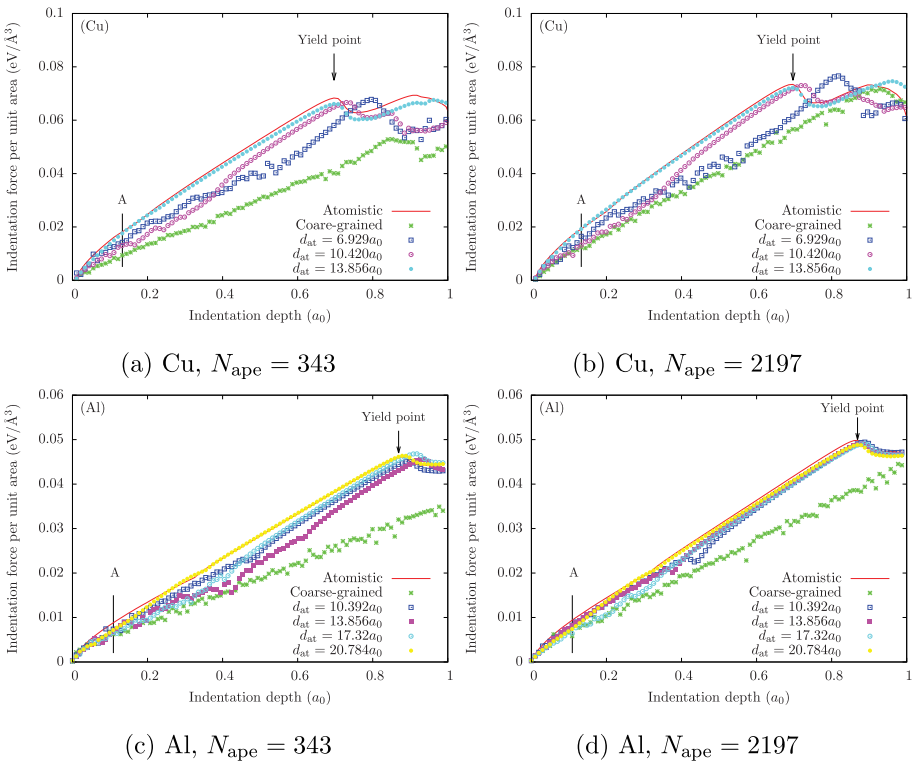

Fig. 13. Indentation force–depth curve obtained from the simulations in both Cu and Al as shown in Fig. 10. The indenter spans along *y* direction over 1 element when $N_{ape} = 2197$ or 2 elements when $N_{ape} = 343$. Free surface atomistic domains with different thickness d_{at} are introduced. The optimal thickness is the smallest d_{at} that results in a monotonically increasing force. It is shown that the optimal d_{at} depends on the materials, but not on the underlying degree of coarse-graining.

To further understand the dislocation dissociation across the interface, a dislocation extraction algorithm (DXA) (Stukowski et al., 2012) is employed to visualize the partial dislocations, as shown in Figs. 17 and 18. It is found that subject to the indentation, a series of 60° mixed type dislocations are nucleated and dissociated into partials with intrinsic stacking fault in between. In Fig. 17a, the dislocation has a correct width in the atomistic domain. With further indentation, the leading partial is first impeded by the domain interface while the trailing partial is unaffected, resulting in a narrower dislocation, as shown in Fig. 17b. Later, the trailing partial is also slowed down by the interface while the leading partial is now migrating steadily in the coarse-graining domain (Fig. 17c). The delay of the partial dislocations is due to the change of the packing sequence in the stacking fault, where the disregistry of atoms are rearranged to have a linear correlation with their positions. It follows that the dislocation becomes wider in the coarse-grained domain, as shown in Fig. 17d. Note that the variation of dislocation width is not observed when the dislocation migrates in an individual domain. Moreover, the averaged dislocation migration velocity in both domains are the same (Xiong et al., 2014b).

When the dislocation migrates from the coarse-grained domain to the atomistic domain, the propagation of both leading and trailing partials are facilitated by the domain interface (Fig. 17e–g) due to a more relaxed environment in full atomistics. Consequently, the dislocation has a correct width once it migrates into the atomistic domain, as shown in Fig. 17h. The domain interface itself, as well as the coarse-grained domain, don't influence the dislocation behaviors in the atomistic domain when the dislocation is not in adjacent to the interface. Similar phenomena are observed in Al, as shown in Fig. 18.

Using the same models, we also study the overall Burgers vector in both fully atomistic and fully coarse-grained domains with varying element size in Al. It is found in Fig. 19 that the non Shockley partial dislocations are nucleated under the indenter in the atomistic domain, while only $(1/6)a_0\langle 112\rangle$ Shockley partials are formed in the coarse-grained domain, due to that the dislocations only migrate between the elements, along which the Burgers vector is smeared. At the same indentation depth $2.62a_0$, the overall Burgers vector of dislocations on the same slip plane are the same in both atomistic and coarse-grained domains. Therefore, the long range stress field of these dislocations is preserved because the dislocation core effect is usually small and local (Bulatov and Cai, 2006). The results using EAM potentials with approximated $\overline{\rho}^j$ proposed in Section 4.4 are only slightly different from those employing EAM potentials with accurate $\overline{\rho}^j$. Similar phenomena are observed in Cu.

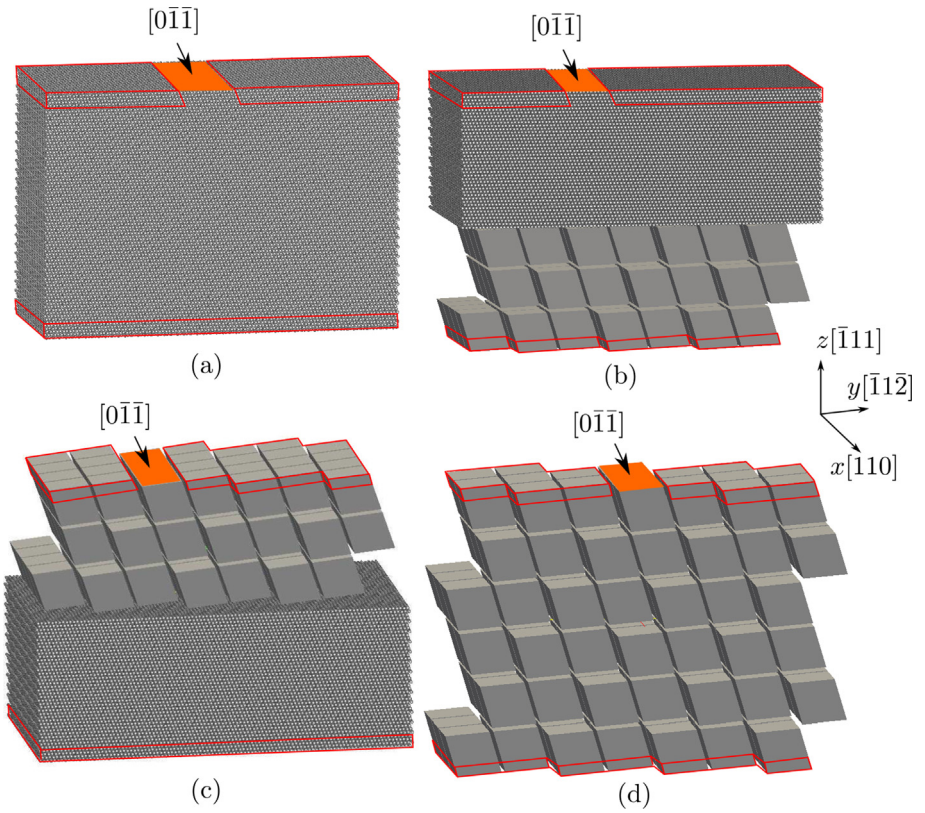

Fig. 14. Four cases comparing the dislocation migration through the interface between atomistic and coarse-grained domains in Cu and Al: (a) fully atomistic case, (b) from atomistic to coarse-grained domain, (c) from coarse-grained to atomistic domain, and (d) fully coarse-grained case. PBCs are applied along both x and y directions. To apply the periodic boundaries in the coarse-grained domain, the jagged interstices are filled in with atoms, which are not shown here. The indenter moves $0.01a_0$ each step in Cu along $[\mathbf{0\bar{1}\bar{1}}]$ direction. The atoms/nodes illustrated by red box are fixed. (For interpretation of the references to colour in this figure legend, the reader is referred to the web version of this article.)

5.5. A preliminary convergence and error analysis

As pointed out by Yang et al. (2014), while many multiscale methods have been proposed, few corresponding convergence and error analyses exist. Some mathematical and/or numerical analyses include, but are not limited to, those of QC (Knap and Ortiz, 2001; Lin, 2003, 2007; Luskin and Ortner, 2009; Van Koten and Luskin, 2011), heterogeneous multiscale method (E and Ming, 2004), bridging scale method (Tang et al., 2006), atomistic-to-continuum coupling (Luskin and Ortner, 2013), and multiresolution molecular statics (Yang et al., 2014). Our previous work (Xiong et al., 2011, 2012b) shows that in dynamic CAC, the coarse-grained domains give closer results to those of the full atomistics when finer elements or larger models are employed. In this section, we present a preliminary convergence and error analysis of quasistatic CAC.

We take the fully atomistic MS result as the "exact solution" that a fully coarse-grained or CAC simulation should be compared with. Thus, the atomistic domain, except the region in adjacent to the atomistic/coarse-grained domain interface, yields an exact result since it employs the same governing equation as MS without interaction with the domain interface. The coarse-grained domain, however, introduces numerical errors due to two main approximations: (1) discretization error by using the trilinear shape function and interpolation function; (2) integration error by dividing an element into subregions and adopting the integration points. The approximations also introduce errors to regions in the atomistic domain that are in the vicinity of the domain interface because of the non-local force/energy. It is beyond the scope of this section to distinguish different sources of error in each domain and perform a comprehensive convergence and error analysis; rather, we will analyze the simulation results to show the convergence and error of quasistatic CAC with respect to MS as a function of (1) ratio of the number of integration points per element to the number of atoms per element, i.e., $N_{\text{ipe}}/N_{\text{ape}}$, (2) element size N_{ape}, and (3) the atomistic domain thickness d_{at} at a surface subject to indentation. The convergence is illustrated by the relative error e_{rel} between two scalars A, i.e.,

$$e_{\text{rel}} = \frac{|A_{\text{cal}} - A_{\text{MS}}|}{|A_{\text{MS}}|} \tag{37}$$

where A_{MS} is the result from MS and A_{cal} is obtained by either fully coarse-grained or CAC simulations.

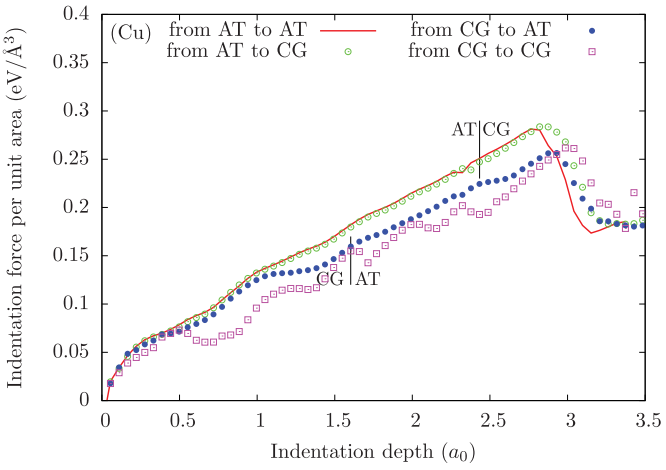

(a) Cu

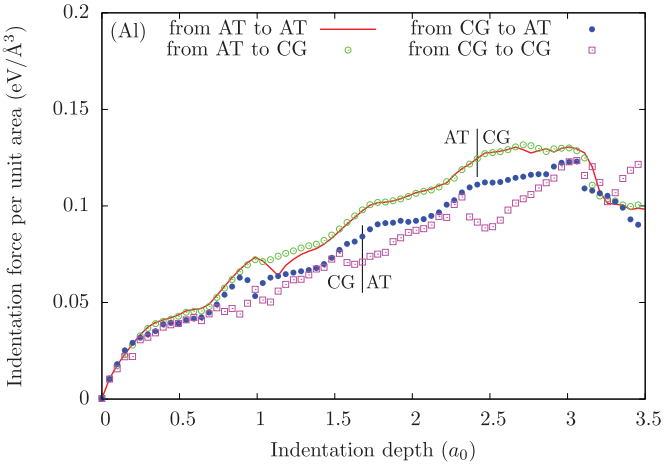

(b) Al

Fig. 15. Indentation force–depth curve obtained from the simulations in both Cu and Al as shown in Fig. 14. No significant change of force is observed when the dislocation migrates across the interface between atomistic and coarse-grained domains.

1. In Section 5.1, the generalized stacking fault energy along $[1\overline{1}2]$ in the coarse-grained domain is calculated using both 1NN and 2NN elements. Each element contains either 2197 or 9261 atoms. The relative errors of both γ_{usf} and γ_{sf} in both Cu and Al decrease to nearly zero when $N_{ipe}/N_{ape} > 0.013$, as shown in Fig. 20. From the perspective of numerical integration, a larger number of integration points yields an exact result for higher order integrand, which is desired for larger element. As N_{ipe}/N_{ape} approaches 1, the integration error tends to disappear while the discretization error still exists. It is shown that for the element sizes studied here, the 2NN type captures well the stacking fault energy in both materials, so extra integration points are not necessary.
2. In Section 5.2, the 60° mixed type dislocation w_d in the coarse-grained domain is calculated using the 2NN elements as a function of the element size N_{ape}. Fig. 21 shows that w_d in both Cu and Al approach the MS results as N_{ape} decreases. The smallest element contains 125 atoms, suggesting that all atoms are taken as integration points and the integration error is zero. However, the total error is not zero because of the existence of the discretization error. With a larger element, the integration errors increase due to a smaller N_{ipe}/N_{ape}. Although the largest element results in a relative error of nearly 1, this doesn't significantly affect the dislocation behaviors in the atomistic domain, as concluded in Section 5.4. In the coarse-grained domain, dislocation mobility approximations are not relevant to quasistatic CAC. As shown in Section 5.4, the net Burgers vector of interelement dislocation and long range stress field are preserved even using the largest element.
3. In Section 5.3, atomistic domains with different thickness d_{at} are employed at the indentation surface. In the underlying coarse-grained domain, each element contains either 343 or 2197 atoms. The indentation force per unit area P_{in} is studied with respect to the indentation depth d_{in} to quantify the free surface effect. We calculate the largest relative

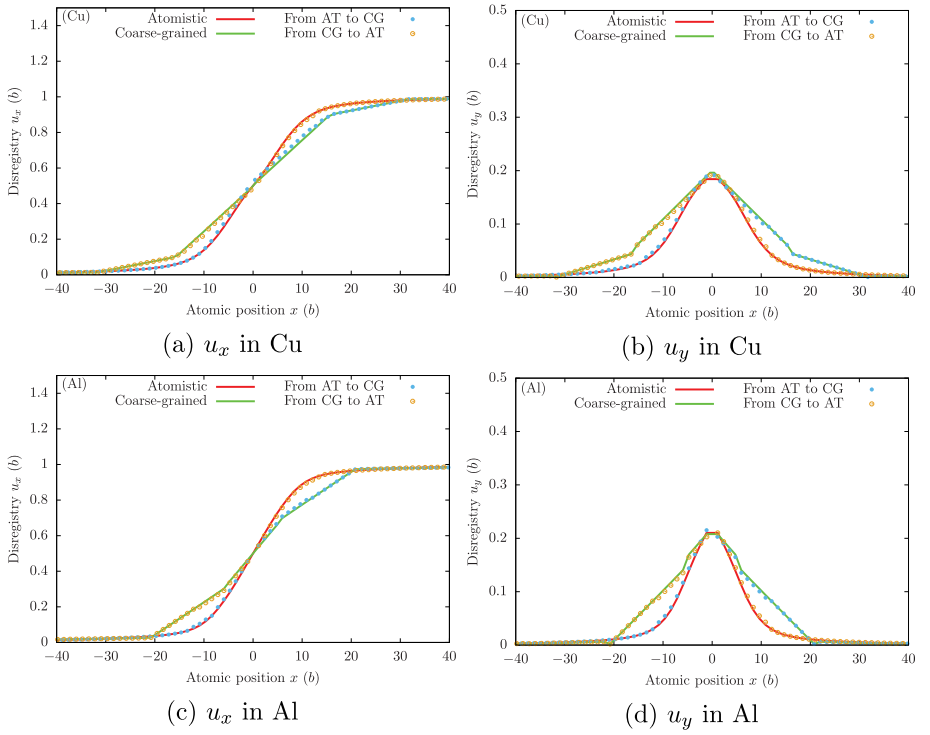

Fig. 16. The 60° mixed type dislocation core is located across the interface ($x = 0$) such that half of it is in the atomistic domain while the other half the coarse-grained domain in both Cu and Al. The disregistry u_x and u_y of dislocation, calculated using the method in Section 5.2, are compared with those in fully atomistic and fully coarse-grained models. The Burgers vector $\mathbf{b} = \mathbf{1/2}\,\boldsymbol{a_0}[\mathbf{110}]$. It is shown that the interface only slightly alters the atomic positions in its vicinity, and the dislocation has a correct core structure once it migrates into the atomistic domain.

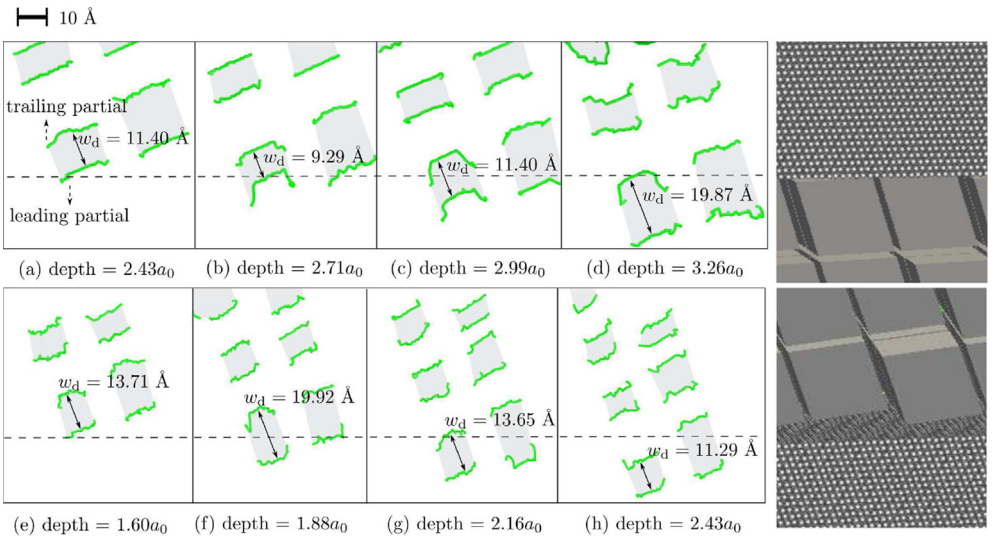

Fig. 17. Snapshots of dislocation migration from the atomistic to coarse-grained domain (a–d), as well as in the opposite direction (e–h) in Cu. The green curves refer to $\mathbf{1/6}\boldsymbol{a_0}\langle\mathbf{112}\rangle$ Shockley partial dislocation lines. The gray ribbons are the intrinsic stacking fault. To apply the periodic boundaries in the coarse-grained domain, the jagged interstices are filled in with atoms, which are not shown here. The domain interface in the first case delays the partials while the one in the second case facilitates the dislocation migration. (For interpretation of the references to colour in this figure legend, the reader is referred to the web version of this article.)

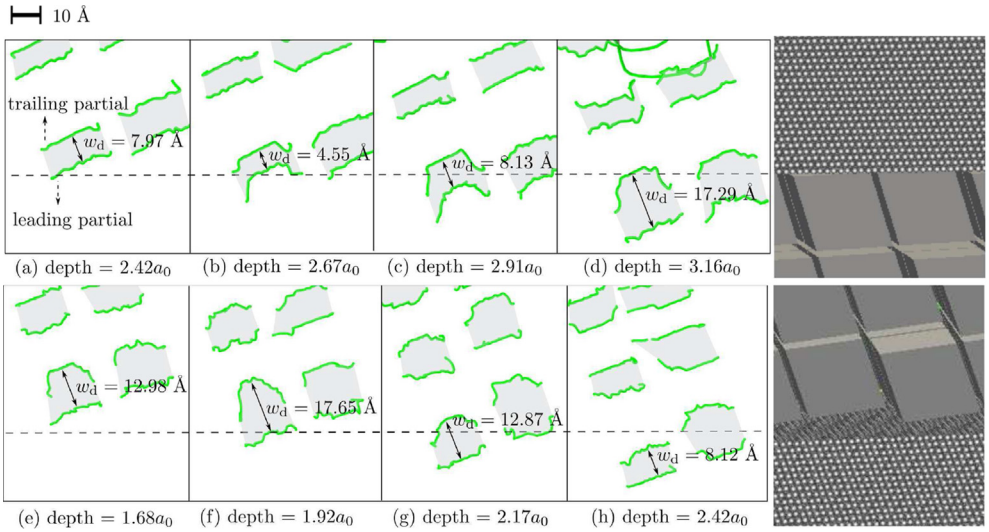

Fig. 18. The same snapshots of dislocation migration as Fig. 17, but in Al. Similar phenomena are observed.

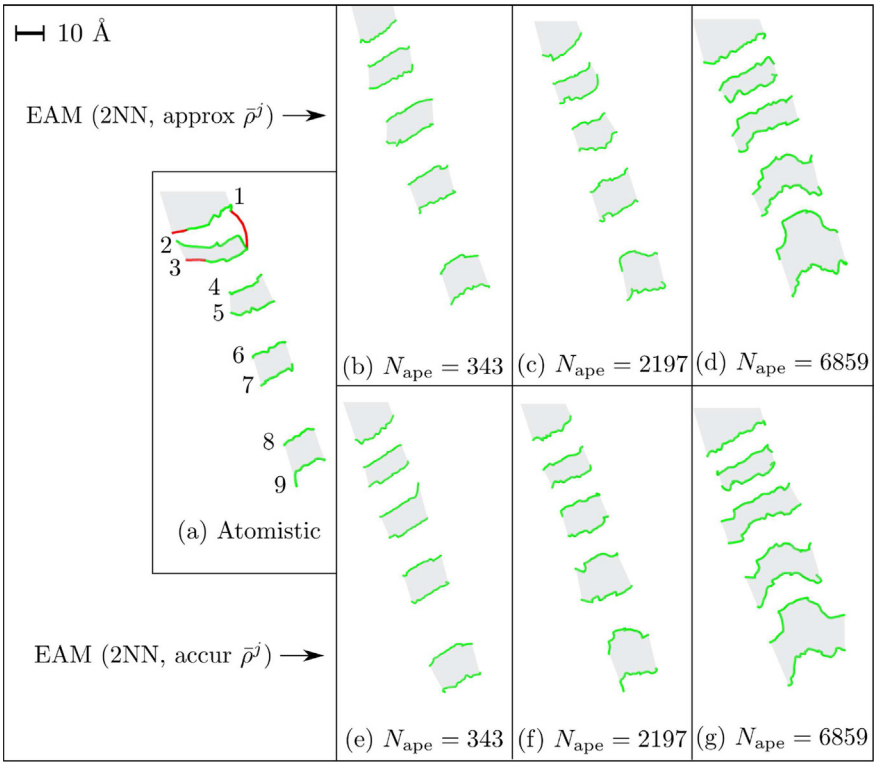

Fig. 19. Snapshots of dislocation migration subject to indentation in both fully atomistic and fully coarse-grained domains with varying element size in Al. The green and red curves refer to $\mathbf{1/6}\,\boldsymbol{a_0}\langle\mathbf{112}\rangle$ Shockley partial and $\mathbf{1/2}\,\boldsymbol{a_0}\langle\mathbf{110}\rangle$ perfect dislocations, respectively. The gray ribbons are the intrinsic stacking fault. It is shown that while only Shockley partials are nucleated in the coarse-grained domain, several non Shockley partials are formed in fully atomistic model. At the same indentation depth $2.62a_0$, the overall Burgers vector of 9 partial dislocations on the same slip plane are the same, regardless of the element size or whether the EAM potential is employed with approximated $\bar{\rho}^j$. (For interpretation of the references to colour in this figure legend, the reader is referred to the web version of this article.)

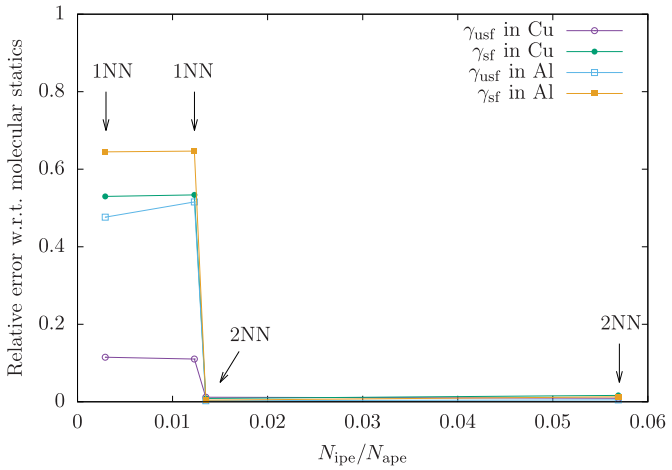

Fig. 20. The relative errors of both γ_{usf} and γ_{sf} in both Cu and Al calculated in the coarse-grained domain using both 1NN and 2NN elements. Each element contains either 2197 or 9261 atoms. The values of stacking fault energy are from Fig. 4. It is shown that the relative errors reduce to nearly zero with increasing $N_{\mathrm{ipe}}/N_{\mathrm{ape}}$.

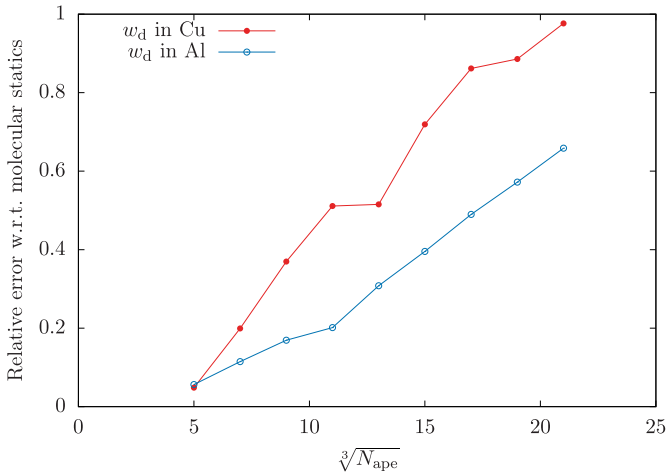

Fig. 21. The relative errors of the 60° mixed type dislocation width w_{d} in both Cu and Al calculated in the coarse-grained domain using 2NN elements with varying element size N_{ape}. The values of w_{d} are from Fig. 7. It is shown that the relative errors reduce to nearly zero with the smallest N_{ape}.

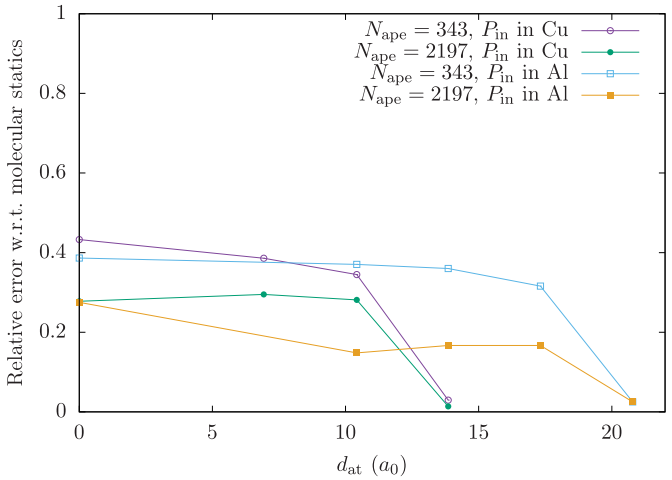

Fig. 22. The largest relative errors of the indentation force per unit area P_{in} between $d_{\mathrm{in}} > 0.1a_0$ and the yield point in both Cu and Al in the nano-indentation simulations. In the underlying coarse-grained domain, each element contains either 343 or 2197 atoms. The values of P_{in} are from Fig. 13. It is shown that the relative errors reduce to nearly zero with the largest d_{at}.

errors of P_{in} between $d_{in} > 0.1a_0$ and the yield point in each case, as shown in Fig. 22. The convergence of P_{in} to the MS result with an increasing d_{at} indicates that the effect of the atomistic/coarse-grained domain interface is negligible at a finite distance.

In summary, a preliminary convergence and error analysis shows that the fully coarse-grained quasistatic implementation provides convergence to fully resolved MS energy minimization by virtue of the inherent consistency of the same underlying interatomic potential in both domains. Similar results are found in two FCC crystalline materials with distinct stacking fault energy.

6. Conclusions

In this paper, the basic formulation of atomistic field theory is reviewed, and a first order quasistatic concurrent atomistic-continuum method is presented. This method is then applied in several benchmark 3-D problems in dislocation plasticity for pure FCC crystals of Cu and Al. Results are summarized as follows:

1. The proposed method partitions the simulation cell into two domains: atomistic and coarse-grained, with atomistic field theory as a unified governing equation. The atomistic domain is solved as in classical molecular statics with sequential energy minimization; in the coarse-grained domain, a finite element method is employed to solve the governing equation in the continuum field that admits discontinuous displacement between elements. Dislocations can pass along these interelement boundaries.
2. The quasistatic CAC method and its implementation are described in detail. Although the algorithm has similarities with full atomistics, some distinctions are addressed, including the choice of the integration points, the force/energy/stress calculation, periodic boundaries, and the parallel computing implementation. The major advantage of the CAC method, compared to other partitioned domain methods, is in the use of interelement discontinuity for dislocation nucleation and migration, facilitating seamless passage of dislocations between atomistic and coarse-grained domains.
3. We explore the capabilities of the quasistatic CAC method by investigating the behavior of dislocations in the coarse-grained domains. First, it is found that the ratio of relaxed stable to relaxed unstable stacking fault energy is lower in the 1NN element, explaining the previous observation in the stress–strain curves that the amplitudes of strain bursts after yielding are larger; second, for a 60° mixed type dislocation, there is a linear correlation between disregistry and atomic position within an element, so the larger the element, the wider the dislocation core and the smaller the maximum magnitude of shear stress; third, the atomistic domain should be applied in place of the coarse-grained domain where the local elastic deformation is significant; fourth, it is shown that the atomistic/coarse-grained domain interface only slightly affects the dislocation migration process and that the overall Burgers vector of dislocations on the same slide plane are the same in both atomistic and coarse-grained domain. Moreover, a preliminary convergence and error analysis shows that the fully coarse-grained quasistatic energy minimized simulations provide satisfying convergence to fully resolved MS energy minimization as the number of atoms per element is reduced.

Both dynamic and quasistatic CAC methods have advantages over most coarse-grained approaches:

1. A unified governing equation and the same interatomic potential are employed in both atomistic and coarse-grained domains, inherently providing the convergence of CAC quasistatic simulations to fully resolved atomistic. Also, since all force/energy calculations are non-local, no ghost forces exist at the atomistic/coarse-grained domain interface in both undeformed and homogeneously deformed configurations.
2. Adaptive remeshing, which is costly and usually employed in multiscale methods to capture lattice defects in the present of continuous elements, is not essential in the current quasistatic CAC implementation, because interelement discontinuity admits the propagation of edge, screw, and mixed character dislocations albeit with a smeared treatment of the dislocation core/Burgers vector. This results in a consistent coarse-graining efficiency compared to MS.
3. Because net Burgers vector and associated long range fields of dislocation arrays are preserved in the coarse-grained domain, CAC coarse graining can be employed in regions remote from defects (e.g., interstitial, vacancy, void, and interfaces), while full atomistic resolution should be employed in the vicinity of defects to reproduce dislocation–defect reactions.

Specifically, the current work contributes to advancing the CAC method in the following ways:

1. The quasistatic approach allows us to describe the precise energy landscape, avoiding issues related to overdriven kinetics in dynamic simulations.
2. The implementation is detailed in a mathematically rigorous matter, where the choice of integration point and Gaussian quadrature are explained. Based on our previous CAC method, 2NN element with first order Gaussian quadrature in each subregion is proposed for the first time, giving an accurate generalized stacking fault energy

without mesh refinement to atomistic scale which, to our knowledge, is beyond the capability of existing coarse-grained methods in the literature.
3. Dislocation core structures in the coarse-grained domain are systematically studied for the first time. Direct evidence is provided to show that the overall Burgers vector and long range stress field of dislocations are preserved.
4. Dislocation migration across the atomistic/coarse-grained domain interface, which is treated artificially in most coarse-grained methods, is explored. Attention is paid in the variation of dislocation core structure across the interface which proves that the interface only slightly affects dislocation migration.
5. The coarse-graining efficiency in one iteration, as well as that of the quasistatic approach, are carefully analyzed. Significant computational benefits are gained using the CAC model relative to the equivalent fully atomistic simulation. Also, a preliminary convergence and error analysis of the CAC method is performed to show that the coarse-grained model converges to fully resolved MS as the element size is decreased.
6. From the computational perspective, several improvements are made based on our previous CAC implementation with regard to parallelization. First, atoms are employed to fill in the jagged interstices to allow periodic simulation cell boundaries; second, in the spatial-decomposition parallelization algorithm, elements are shared between neighboring processors, each of which only calculates force/energy of the integration points within its own domain — parallel efficiency is thus improved; third, the host electron density of atoms within the same subregion is assumed constant, facilitating application of the EAM potential; last, the spatially unbalanced work load between processors, which is a common issue in multiscale modeling, is alleviated by adaptively assigning approximately the same number of "evaluation points" to different processors.

However, because the dislocation paths are confined to lie along interelement boundaries, not all types of defects can be captured in the coarse-grained domain. For instance, complex extended core interactions cannot be accurately described. Future development of the quasistatic implementation of CAC described in this paper will consider adaptive mesh refinement, higher order shape/interpolation functions, and enrichment functions within elements to admit dislocations in element interior regions (Belytschko et al., 2009). While all computations in this work use 3-D models, we leave the study of larger domains and larger scale curved dislocations of mixed character to future work.

The purpose of this paper is to compare quasistatic CAC with MS simulations to demonstrate its capability in describing individual dislocations in the coarse-grained domain, as a prelude to modeling large numbers of dislocations. It is not our intent here to shed light on improved understanding of dislocation core level phenomena, but rather to establish that the method adequately replicates essential aspects of dislocation fields. For example, an issue of great relevance that challenges the length scale limits of classical atomistic simulations is the multiple, successive reactions of leading dislocations in long range pile-ups against atomistically resolved grain boundaries or interfaces. Exploring this matter using quasistatic CAC and providing a comprehensive convergence and error analysis involving different integration schemes are left to future research.

Acknowledgments

This material is based upon work supported by the National Science Foundation as a collaborative effort between Georgia Tech (CMMI-1232878) and University of Florida (CMMI-1233113). Any opinions, findings, and conclusions or recommendations expressed in this material are those of the authors and do not necessarily reflect the views of the National Science Foundation. The authors would like to thank Dr. Jonathan Zimmerman, Dr. Mark Tschopp, Dr. Shreevant Tiwari, and Dr. Shengfeng Yang for helpful discussions, and Dr. Alexander Stukowski for providing the dislocation extraction algorithm code. This work used the Extreme Science and Engineering Discovery Environment (XSEDE), which is supported by National Science Foundation grant number ACI-1053575.

Appendix A. Equivalent nodal force

The displacement field $\mathbf{u}$ is the difference between the reference and current configurations, i.e.,

$$\mathbf{u}(\mathbf{X},t) = \mathbf{r}(\mathbf{X},t) - \mathbf{X} \tag{A.1}$$

where $\mathbf{X}$ denotes the position of a material point in the reference configuration. So we have

$$\ddot{\mathbf{r}} = \ddot{\mathbf{u}}. \tag{A.2}$$

In the quasistatic implementation of CAC, there is no dynamic or inertial effects, so the accelerations of the atoms/nodes are zero and the inertia effect, which involves both the atomic mass in the atomistic domain and the mass matrix in the coarse-grained domain, doesn't influence the simulation result. In the following sections, however, the acceleration and mass are employed as a means to relate the continuum and atomistic domains and derive the equivalent nodal force in Eq. (12), which does not depend on acceleration nor mass.

We apply the weighted residual method by substituting Eq. (A.2) into Eq. (1), multiplying the latter equation by a weight function Φ_ν, and performing the integration over the simulation domain Ω, i.e.,

$$\int_{\Omega(\mathbf{r})} \left[\rho\Phi_\nu(\mathbf{r})\mathbf{\Phi}_\xi(\mathbf{r})\ddot{\mathbf{u}}_\xi - \Phi_\nu(\mathbf{r})\mathbf{f}_{\text{int}}(\mathbf{r})\right] d\Omega(\mathbf{r}) = \mathbf{0} \quad \nu = 1, 2, \ldots, N_{\text{npe}}. \tag{A.3}$$

The Galerkin method is employed, by taking the shape function as the weight function. Eq. (A.3) can be viewed as a system of equations for the (time varying) nodal displacements for the dynamic problem derived by the principle of virtual work. The second term is the internal force that causes the nodal displacement. Since here we don't integrate by parts to decrease the continuity requirement on $\mathbf{u}$, Eq. (A.3) is not a weak form.

Writing Eq. (A.3) in matrix form, the first term becomes

$$\int_{\Omega(\mathbf{r})} \rho\mathbf{\Phi}_\nu(\mathbf{r})\mathbf{\Phi}_\xi(\mathbf{r})\ddot{\mathbf{u}}_\xi d\Omega(\mathbf{r}) = \mathbf{M}\ddot{\mathbf{u}}_\xi = \mathbf{M}\ddot{\mathbf{R}}^\xi \tag{A.4}$$

where $\mathbf{\Phi}_\nu$ is an $N_{\text{npe}} \times 1$ vector, $\mathbf{R}^\xi$ is a $N_{\text{npe}} \times 3$ matrix, and

$$\mathbf{M} = \int_{\Omega(\mathbf{r})} \rho\mathbf{\Phi}_\nu(\mathbf{r})\mathbf{\Phi}_\xi(\mathbf{r}) d\Omega(\mathbf{r}) \tag{A.5}$$

is a $N_{\text{npe}} \times N_{\text{npe}}$ local mass matrix.

The second term of Eq. (A.3) can be replaced by a quadrature, i.e.,

$$\int_{\Omega(\mathbf{r})} \mathbf{\Phi}_\nu(\mathbf{r})\mathbf{f}_{\text{int}}(\mathbf{r}) d\Omega(\mathbf{r}) = \sum_{\mu}^{N_{\text{ipe}}} \omega'_\mu \mathbf{\Phi}_{\mu\nu}\mathbf{f}_\mu \tag{A.6}$$

where ω'_μ are the quadrature weight in terms of force density, $\mathbf{\Phi}_{\mu\nu}$ is a $N_{\text{npe}} \times 1$ vector, and $\mathbf{f}_\mu$ is a 1×3 vector. While integration points μ can correspond to any material point in the continuum, we let μ correspond to actual atoms. In this way, the calculation of force/energy is straightforward, as indicated in Section 2.2. It follows that

$$\mathbf{f}_\mu = \frac{\mathbf{F}^\mu}{\Omega^\mu} \tag{A.7}$$

where 1×3 vector $\mathbf{F}^\mu$ is the atomic force at μ and Ω^μ is the volume of μth integration point.

Substituting Eqs. (A.4), (A.6), and (A.7) into Eq. (A.3) leads to

$$\mathbf{M}\ddot{\mathbf{R}}^\xi - \sum_\mu \omega_\mu \mathbf{\Phi}_{\mu\nu}\mathbf{F}^\mu = \mathbf{0} \tag{A.8}$$

where ω_μ, the quadrature weight in terms of atomic force, is related to ω'_μ by

$$\omega_\mu = \frac{\omega'_\mu}{\Omega^\mu}. \tag{A.9}$$

Changing the dummy index ν to ξ, Eq. (A.8) becomes

$$m^\xi \ddot{\mathbf{R}}^\xi - \mathcal{F}^\xi = \mathbf{0} \tag{A.10}$$

where

$$\mathcal{F}^\xi = m^\xi \mathbf{M}^{-1} \sum_\mu \omega_\mu \mathbf{\Phi}_{\mu\xi}\mathbf{F}^\mu. \tag{A.11}$$

Here, $\mathcal{F}^\xi$, a $N_{\text{npe}} \times 3$ matrix, is the equivalent nodal force on nodes ξ. To ensure that $\mathcal{F}^\xi$ is on the order of atomic force, we require

$$\mathcal{F}^\xi = \frac{\sum_\mu \omega_\mu \Phi_{\mu\xi} F^\mu}{\sum_\mu \omega_\mu \Phi_{\mu\xi}} \tag{A.12}$$

which is the equivalent nodal force formulation in Eq. (12).

Comparing Eq. (A.11) with Eq. (A.12), we must satisfy

$$m^{\xi}\mathbf{M}^{-1}\sum_{\mu}\omega_{\mu}\mathbf{\Phi}_{\mu\xi}=\mathbf{\Gamma} \tag{A.13}$$

where $\mathbf{\Gamma}$ is a $N_{\text{npe}}\times 1$ matrix with all elements unity. Equivalently,

$$\sum_{\mu}\omega_{\mu}\mathbf{\Phi}_{\mu\xi}=\frac{\mathbf{M\Gamma}}{m^{\xi}} \tag{A.14}$$

where $\mathbf{M\Gamma}$ is a $N_{\text{npe}}\times 1$ matrix, whose elements are the sum of rows in $\mathbf{M}$. We use a lumped mass matrix, whose diagonal elements of its inverse matrix $\mathbf{M}^{-1}$ are $N_{\text{npe}}/(m^{\xi}N_{\text{ape}})$. Then, for each node ξ

$$\sum_{\mu}\omega_{\mu}\Phi_{\mu\xi}=\frac{N_{\text{ape}}}{N_{\text{npe}}}. \tag{A.15}$$

Appendix B. Integration points

While multiple choices of integration points μ and weight ω_{μ} satisfy Eq. (A.15), we take the liberty to further restrict that

$$\sum_{\mu}\omega_{\mu}=N_{\text{ape}} \tag{B.1}$$

such that the total weight of the integration points within one element is the number of atoms it contains. The integration points play a similar role to the sampling atoms used in other concurrent multiscale methods such as virtual atom cluster (Qian and Gondhalekar, 2004), atom collocation method (Yang et al., 2012), and multiresolution molecular mechanics (MMM) (Yang et al., 2013a; Biyikli et al., 2014). In these methods, the computational demand is reduced by only calculating the force/energy of the sampling points, and Eq. (B.1) is usually satisfied.

In Eq. (A.6), the integral is approximated by a weighted sum of the evaluations of the integrand at a set of integration points μ. In numerical integration, the positions and weights of μ are usually determined by the order of the integrand. It is, however, difficult to employ a unified set of integration points within an element due to two reasons:

1. The integrand $\mathbf{\Phi}_{\nu}(\mathbf{r})\mathbf{f}_{\text{int}}(\mathbf{r})$ can be a complicated and highly non-linear function of $\mathbf{r}$, whose order is usually difficult to anticipate *a priori*.
2. The varying of the integrand is not uniform within an element. Among all atoms, those close to the element surface can better "feel" what happens outside, i.e., their force/energy are more sensitive to external influences. In contrast, the remaining "interior atoms" are arranged in a similar local lattice structure decided only by the element's overall deformation through a trilinear interpolation function. For example, assume that an element initially represents a perfect lattice, where all atoms have the same force/energy. When a dislocation propagates between elements, the force/energy of each "surface atom" varies substantially while those of the "interior atoms" remain nearly the same.

To circumvent this problem, we divide one element into a number of non-overlapping subregions, as shown in Fig. B.23. In this way, we only need to determine the order of the integrand within each subregion, which is usually lower than that within the whole element and is more easily approximated. The integration in Eq. (A.6) becomes

$$\int_{\Omega(\mathbf{r})}\mathbf{\Phi}_{\nu}(\mathbf{r})\mathbf{f}_{\text{int}}(\mathbf{r})\mathrm{d}\Omega(\mathbf{r})=\sum_{\alpha}^{N_{\text{spe}}}\int_{\Omega_{\alpha}(\mathbf{r})}\mathbf{\Phi}_{\nu}(\mathbf{r})\mathbf{f}_{\text{int}}(\mathbf{r})\mathrm{d}\Omega_{\alpha}(\mathbf{r})=\sum_{\alpha}^{N_{\text{spe}}}\sum_{\mu}^{N_{\text{ips}}}\omega'_{\mu}\mathbf{\Phi}_{\mu\nu}\mathbf{f}_{\mu} \tag{B.2}$$

where Ω_{α} is the volume of subregion α, N_{spe} the number of subregions per element, and N_{ips} the number of integration points per subregion. The accuracy of the quadrature in Eq. (A.6) depends on (1) how the element is divided and (2) whether the evaluations at the integration points can *represent* that of all atoms in the same subregion. Below, we first discuss the integration within one subregion as this determines the division of the element.

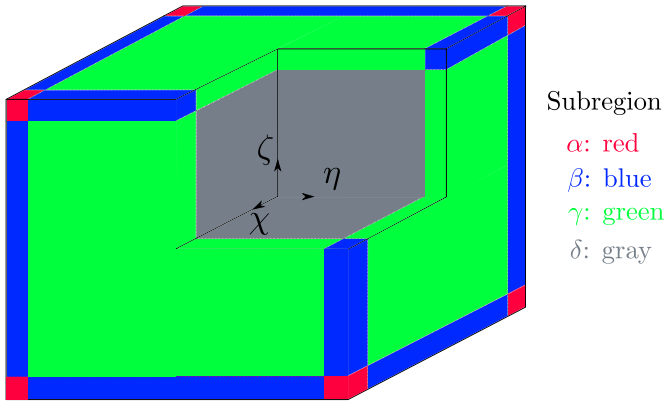

Fig. B.23. 3-D illustration of the subregions within an element in natural coordinates in CAC simulations. The atoms are not shown. Four types of subregions, α, β, γ, and δ, are marked in red, blue, green, and gray, respectively. Within each subregion there is one integration point, as shown in Fig. B.26. The same type of subregion contains different numbers of atoms in 1NN and 2NN elements, so the relevant integration points have different weights, according to Eq. (B.8). The "surface atoms" are located in subregions α, β, and γ, while the "interior atoms" are contained by subregion δ. (For interpretation of the references to colour in this figure legend, the reader is referred to the web version of this article.)

The integrand $\mathbf{\Phi}_\nu(\mathbf{r})\mathbf{f}_{\text{int}}(\mathbf{r})$ in Eq. (A.6) is a $N_{\text{npe}} \times 3$ matrix, i.e.,

$$\begin{bmatrix} \Phi_1 \\ \vdots \\ \Phi_{N_{\text{npe}}} \end{bmatrix} \cdot \begin{bmatrix} f_{\text{int}}^{\chi} & f_{\text{int}}^{\eta} & f_{\text{int}}^{\zeta} \end{bmatrix} = \begin{bmatrix} \Phi_1 f_{\text{int}}^{\chi} & \Phi_1 f_{\text{int}}^{\eta} & \Phi_1 f_{\text{int}}^{\zeta} \\ \vdots & \vdots & \vdots \\ \Phi_{N_{\text{npe}}} f_{\text{int}}^{\chi} & \Phi_{N_{\text{npe}}} f_{\text{int}}^{\eta} & \Phi_{N_{\text{npe}}} f_{\text{int}}^{\zeta} \end{bmatrix}. \tag{B.3}$$

Taking the first element $\Phi_1 f_{\text{int}}^{\chi}$ of the matrix as an example, we assume that within each subregion, the force density is quasi-constant, i.e.,

$$f_{\text{int}}^{\chi}(\mathbf{r}) = f_{\mu}^{\chi} \tag{B.4}$$

except at the boundary, because different subregions have a different f_{μ}^{χ} which is continuous at the boundary. Moreover, since the force density is related to the deformation gradient, the assumption only applies when the deformation gradient remains nearly the same within an element, regardless of the order of the shape function. In practice, however, the force density gradient within the subregion boundary is small because it is essentially calculated between two neighboring atomic sites. So the boundary effect is negligible. Within subregion α, the integral on the first element in Eq. (B.3) becomes

$$\int\limits_{\Omega_\alpha(\mathbf{r})} \Phi_1(\mathbf{r}) f_{\text{int}}^{\chi}(\mathbf{r}) \mathrm{d}\Omega_\alpha(\mathbf{r}) = f_{\mu}^{\chi} \int\limits_{\Omega_\alpha(\mathbf{r})} \Phi_1(\mathbf{r}) \mathrm{d}\Omega_\alpha(\mathbf{r}) \tag{B.5}$$

where the shape function for node 1, $\Phi_1(\mathbf{r})$, is trilinear with respect to $\mathbf{r}$, regardless of the subregion. The Gaussian quadrature rule suggests that in 1-D integration on interval $[a,b]$, one integration point located at $b + a/2$ with weight $(b - a)$ can yield an exact result for a linear polynomial integrand (Chapra and Canale, 2009). Thus in this paper, the 1st order Gaussian quadrature is employed for the numerical integration. A higher order Gaussian quadrature is desired if the force density varies within each subregion and/or a higher order shape function is employed; the exact force density function within a subregion depends on both the size/position of the subregion and the interatomic potentials. For 2-D integration within a subregion illustrated in Fig. B.24, the interval along χ and η directions are $[-(N_\chi + 1/2)a_0/2, (N_\chi + 1/2)a_0/2]$ and $[-(N_\eta + 1/2)a_0/2, (N_\eta + 1/2)a_0/2]$, respectively. Thus, the integration point should be located at (0,0) with weight

$$\omega'_\mu = \omega'_\chi \omega'_\eta = \left(N_\chi + \frac{1}{2}\right)\left(N_\eta + \frac{1}{2}\right) a_0^2. \tag{B.6}$$

In a 2-D subregion, Ω^μ is the area of a unit cell in natural coordinates, i.e.,

$$\Omega^\mu = \frac{a_0^2}{4}. \tag{B.7}$$

Substituting Eqs. (B.6) and (B.7) into Eq. (A.9), we have

$$\omega^{\mu} = (2N_{\chi} + 1)(2N_{\eta} + 1), \tag{B.8}$$

which suggests that the weight of an integration point is the number of atoms within the same subregion. The same conclusion can be obtained for a 3-D subregion. Equation (B.1) is therefore satisfied.

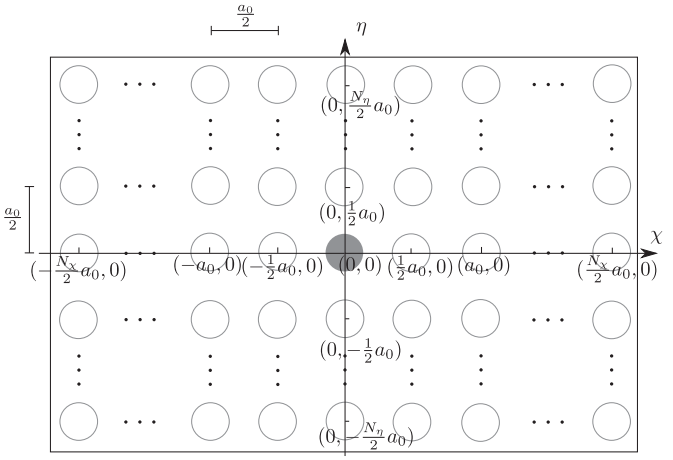

Fig. B.24. Illustration of a 2-D subregion containing $(2N_\chi + 1) \times (2N_\eta + 1)$ atoms in natural coordinates. The filled circle in the origin is the integration point. The open circles are non-integration point atoms. The boundaries of the subregion along χ and η directions are $[-(\mathbf{N}_\chi + \mathbf{1/2})\boldsymbol{a_0}/\mathbf{2}, (\mathbf{N}_\chi + \mathbf{1/2})\boldsymbol{a_0}/\mathbf{2}]$ and $[-(\mathbf{N}_\eta + \mathbf{1/2})\boldsymbol{a_0}/\mathbf{2}, (\mathbf{N}_\eta + \mathbf{1/2})\boldsymbol{a_0}/\mathbf{2}]$, respectively. Note that in the field description of an element, an integration point can be any continuum point. In this paper, we choose the actual atoms because the force/energy calculation is straightforward.

Equation (B.4) suggests that the force density field within one element is approximated by a piecewise constant function. To ensure that the approximation is accurate, we first need to determine the spatial variation of atomic force $\mathbf{F}^k$, which is related to the force density by a constant via Eq. (7), within one element. Then we identify a coarse subregion with large number of atoms where the atomic force doesn't vary much, and a fine subregion where the atomic force has a substantial gradient. We notice that although the force/energy caused by one atom is effective at an infinitely large distance, the interaction between a pair of atoms is negligible when separated farther than a cutoff distance r_c. In particular, for the EAM potentials employed in this paper, the force/energy changes very little beyond the second nearest neighbor (2NN) and third nearest neighbor (3NN) distances, respectively, as shown in Fig. B.25. This suggests that to provide a reasonable approximation for energy minimization, the atoms beyond 2NN distance from the element surface can be taken as “interior atoms”. We validate this assumption quantitatively in Section 5.1.

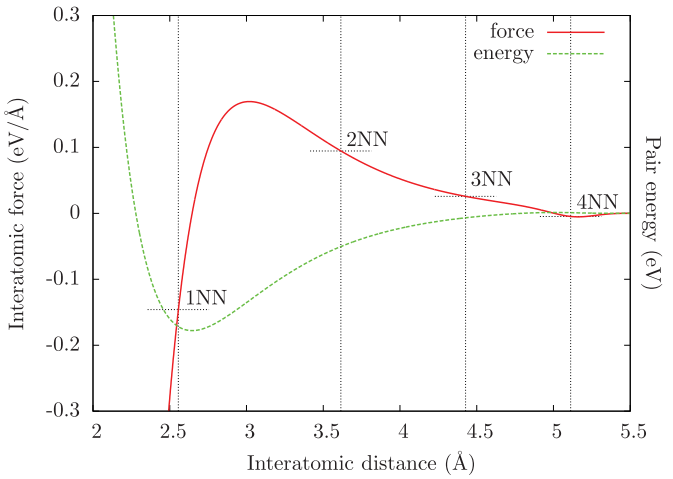

Fig. B.25. The interatomic force and pair energy are calculated using the Cu EAM potential (Mishin et al., 2001) with respect to the interatomic distance. Change in the pair energy is negligible when the interatomic distance is beyond the 2NN distance, whereas change in the force is negligible beyond the 3NN distance. This suggests that sampling atoms within 2NN distance from the element surface may provide a reasonable approximation for energy minimization. The same can be said for Al. Note that the host electron density is assumed constant, so only the force contribution from the pair potential is shown here.

Following these ideas, we develop two types of elements: 1NN and 2NN elements in CAC simulations. Fig. B.26 illustrates the division of subregions in a 2-D element, with gray representing the "interior atoms", both red (nodes) and blue the "surface atoms". A coarse subregion is employed to contain all "interior atoms" because they are beyond a certain distance from the element surface along both χ and η directions and are assumed to have the same force/energy. For the "surface atoms", more highly resolved subregions are adopted. Note that some atoms, e.g., atom β, lie on the surface along the η direction but are far from the surface in terms of the χ direction. We can then assume that atom β and atoms in similar positions (e.g., β_1 and β_2) have the same force/energy and so they are in the same subregion.

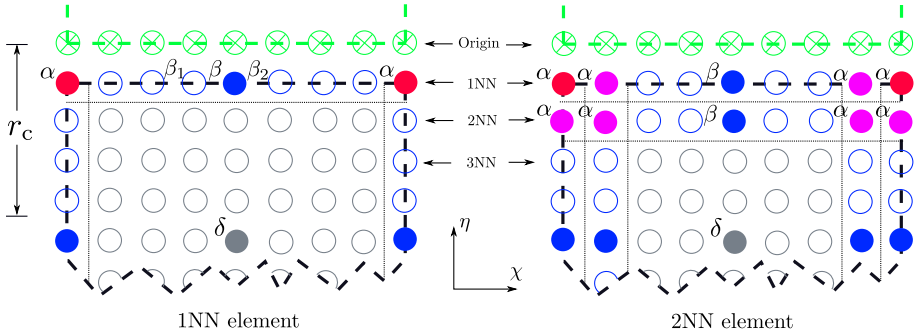

Fig. B.26. 2-D illustrations of part of a 1NN and a 2NN element in natural coordinates in CAC simulations. r_c is the cutoff distance of the interatomic potential. The element is divided into a number of subregions by dotted lines, each of which contains one integration point (filled circle) that is located in the center of the subregion. The gray circles are the "interior atoms" and both red and blue are the "surface atoms". The red circles are also the nodes from which all atoms within an element are interpolated. Within a 3-D element, there are 27 and 125 integration points in a 1NN and a 2NN element, respectively, regardless of the element size. (For interpretation of the references to colour in this figure legend, the reader is referred to the web version of this article.)

As illustrated in Fig. B.23, four types of subregions in a 3-D element, α, β, γ, and δ, are marked in red, blue, green, and gray, respectively. Except subregion type α which only contains one atom, the same type of subregion contains different numbers of atoms in 1NN and 2NN elements, and so the relevant integration points have different weights, according to Eq. (B.8). In general, the subregions are located symmetrically with respect to the axes in natural coordinates and the integration points are in the center of the subregion; we therefore require that the subregions and elements have an odd number of atoms along each axis. The number of each type of subregion and weight of relevant integration points in a 3-D element are shown in Table B.2. Within each element, there are 27 and 125 integration points for 1NN and 2NN types, respectively, regardless of N_{ape}. Equation (B.1) holds for both element types, i.e., for a 1NN element,

$$8 + 12 \times \left(\sqrt[3]{N_{\text{ape}}} - 2\right) + 6 \times \left(\sqrt[3]{N_{\text{ape}}} - 2\right)^2 + \left(\sqrt[3]{N_{\text{ape}}} - 2\right)^3 = N_{\text{ape}} \tag{B.9}$$

and for a 2NN element,

$$64 + 48 \times \left(\sqrt[3]{N_{\text{ape}}} - 4\right) + 12 \times \left(\sqrt[3]{N_{\text{ape}}} - 4\right)^2 + \left(\sqrt[3]{N_{\text{ape}}} - 4\right)^3 = N_{\text{ape}}. \tag{B.10}$$

In both types of elements, the "surface atoms" and "interior atoms" are treated differently, as explained above. However, two layers of atoms are in the "surface" of the 2NN element, compared to only one layer of atoms in the 1NN element. Consequently, the 2NN element better captures the variation of force/energy due to the interelement displacement discontinuity (e.g., dislocations), and so better describes the associated surface rearrangement/reconstruction. In practice, elements in the vicinity of a free surface and dislocations should be of 2NN type, while those in perfect lattice can be of 1NN type to reduce the computational intensity. Moreover, since the justification of the 2NN element is based on the interatomic force/energy–distance relation, the proper thickness of the "surface" region depends on the interatomic potential. For example, for a long range interatomic potential, we need elements with a thicker "surface" region.

Note that although the integration points in CAC are analogous to the sampling points, e.g., in MMM, they don't serve the same purpose. MMM is a coarse-grained atomistic method with no continuum concept such as stress or strain employed in its framework (Yang et al., 2014), while CAC is based on a continuous field theory. It is also noteworthy to mention that in our earlier work, both nodal integration (Deng et al., 2010) and 2nd order Gaussian quadrature (Xiong et al., 2011, 2012b,a,c, 2014a,b, 2015; Deng and Chen, 2013; Yang et al., 2013b) are employed. The 2nd order Gaussian quadrature in CAC also divides a 3-D element into subregions as in Fig. B.23 and the positions of each type of subregion are similar to those in the 1NN element. However, the positions and weights of the integration points are different from those presented in Table B.2. In this

paper, the subregions are divided such that the 1st order Gaussian quadrature yields exact solutions based on our assumptions, with 1 integration point in each subregion compared with 2^n in the 2nd order Gaussian quadrature where n is an integer between 0 and 3.

Table B.2
Number of each type of subregion and weight of relevant integration points in 3-D 1NN and 2NN elements.

Element type		Subregion type			
		α	β	γ	δ
1NN	Number	8	12	6	1
	Weight	1	$\sqrt[3]{N_{\text{ape}}}-2$	$(\sqrt[3]{N_{\text{ape}}}-2)^2$	$(\sqrt[3]{N_{\text{ape}}}-2)^3$
2NN	Number	64	48	12	1
	Weight	1	$\sqrt[3]{N_{\text{ape}}}-4$	$(\sqrt[3]{N_{\text{ape}}}-4)^2$	$(\sqrt[3]{N_{\text{ape}}}-4)^3$

Appendix C. CAC algorithm

Due to the similarity between CAC and MS simulations regarding lattice structure and force/energy calculations, the CAC algorithm adopts common MS techniques. Newton's third law is employed in the atomistic domain to promote efficiency in calculating the force, pair potential, local electron density, and stress. The short-range neighbor search adopts a combined Verlet list (Verlet, 1967) and link-cell (Allen and Tildesley, 1989) methods. The CAC simulations run in parallel using Message Passing Interface (MPI). We choose the spatial-decomposition algorithm because of its minimized amount of data communication (Plimpton, 1995).

There are four major issues in CAC simulations with coarse-graining that don't exist in standard MS:

1. In the coarse-grained domain, the surfaces of the rhombohedral elements correspond to {111} planes. While facilitating the description of dislocation nucleation and migration, this prevents us from constructing a parallelepipedonal coarse-grained domain with arbitrary lattice orientations relative to surfaces of the overall simulation cell. If we only use rhombohedral elements in the model, the simulation box will most likely have jagged boundaries, as shown in Fig. C.27a. To facilitate application of PBCs, we can fill in the jagged interstices at simulation cell boundaries with atoms, as shown in Fig. C.27b.
2. Another issue in PBCs implementation is that an object crossing through one face of the simulation box should enter the box through the opposite face. In atomistic simulations, this is realized via displacing the atoms by the box lengths along the directions along which PBCs are applied. In the coarse-grained domain, however, care must be taken when not all nodes of one element are displaced, i.e., an element is cut through by a periodic boundary. In this case, the nodal positions should be reinstated to interpolate the positions of atoms within the element. Subsequently, the reinstated nodes and some of the interpolated atoms are displaced following the PBC algorithm. The procedure is shown in Fig. C.28.
3. In CAC quasistatic simulations with both atomistic and coarse-grained domains, only the force/energy/host electron density of the integration points and atoms (referred to as evaluation points) are computed, so the workload, which is proportional to the number of interactions, is poorly balanced if we assign each processor an equally-sized cubic domain as in full atomistics (Pearce et al., 2014). Since the local density of interactions doesn't significantly vary within the simulation cell, we use the number of evaluation points as an approximation of the workload and assign each processor domain approximately the same number of evaluation points, which is re-evaluated at regular time intervals (Bulatov et al., 2004). It follows that at periodic boundaries filled in with atoms or in the vicinity of lattice defects where full atomistics is employed, the processors are assigned smaller domains that contain more atoms than other processors whose domains contain more nodes.
4. In Fig. C.27c, element 1 is shared between processors P_1, P_2, P_4, and P_5. This overlapping domain is common in parallel finite element implementations. We use the algorithm described below to address the shared element implementation.
   (a) For element 1, P_1, P_2, and P_5 contain some non-overlapping integration points while processor P_4 doesn't have any integration point. One processor, e.g., P_1, is chosen as the host processor for this element.
   (b) P_1, P_2, and P_5 calculate the force/energy of its own integration points, which are then sent to P_1.
   (c) P_1 calculates the equivalent nodal force/energy of this element based on the data it receives from the other processors using Eq. (A.11) and Eq. (22).
   (d) P_1 varies the nodes along a certain direction (which is a function of the equivalent nodal force) before sending the updated nodal positions to all other processors.
   (e) Note that in Fig. C.27c, although processors P_4 doesn't contain any integration points but only a non-integration point atom k, it still needs to access the updated nodal positions from P_1. This is because the position of k is needed by other atoms P_4 contains in doing the non-local force/energy calculations.

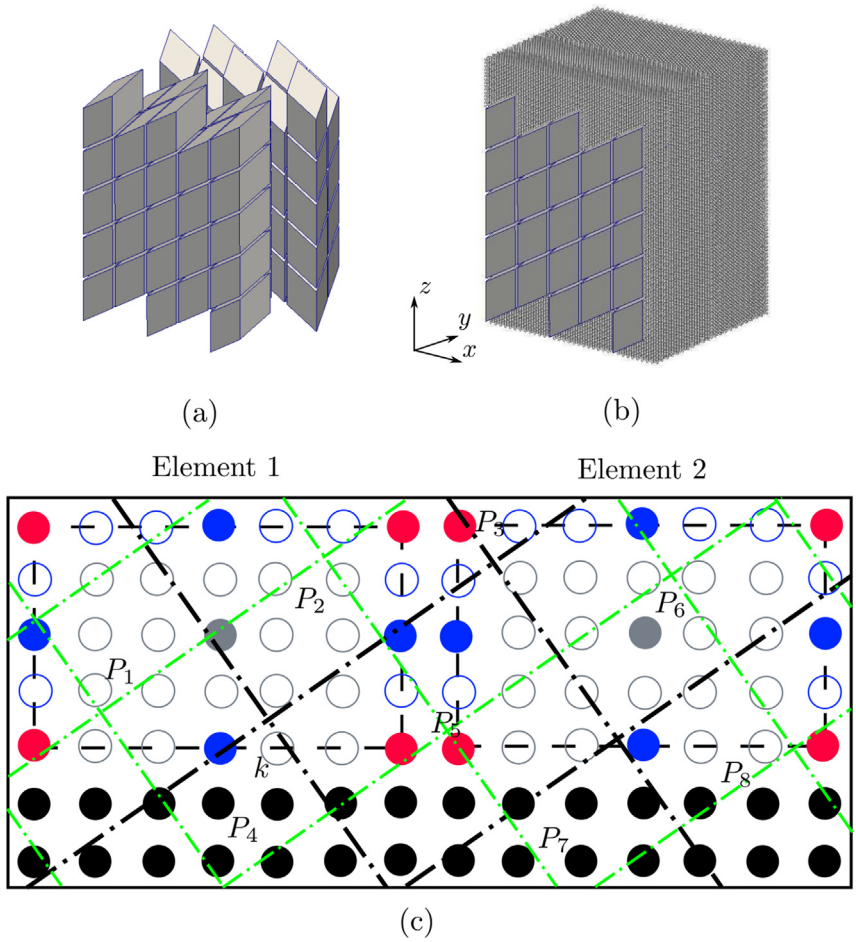

Fig. C.27. (a) A simulation cell consists of only elements, with jagged boundaries. (b) Atomistic domains are introduced to "fill in" the interstices between planar boundaries of a cubic simulation cell and element boundaries. (c) 2-D Illustration of dividing a simulation cell containing 2 elements and 28 atoms in natural coordinates into a number of link-cells (green and black dot-dash lines) and processor domains (black dot-dash lines). Elements are illustrated by black dash lines, where red (nodes), blue, and gray filled circles are integration points, open circles are non-integration point atoms. The black filled circles are atoms in the atomistic domain. (For interpretation of the references to colour in this figure legend, the reader is referred to the web version of this article.)

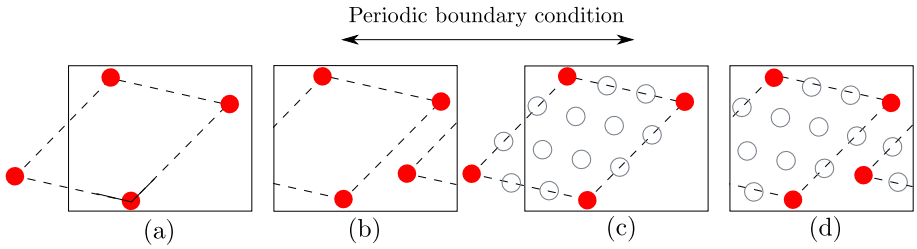

Fig. C.28. A 2-D illustration of a simulation cell with PBCs along the direction marked by an arrow. Red filled circles are nodes and gray open circles are interpolated atoms within an element which is illustrated by black dash lines. (a) An element is cut through by the periodic boundary with one node crossing the left boundary. (b) It follows that the node enters the simulation box through the right boundary. (c) In interpolating the positions of atoms within the element, the nodal position is reinstated. (d) Subsequently, the node and some interpolated atoms are displaced following the PBC algorithm. (For interpretation of the references to colour in this figure legend, the reader is referred to the web version of this article.)

Although the employment of discontinuous elements in CAC simulation results in a larger number of nodes for an identical number of elements relative to a continuous formulation, it shares advantages with the discontinuous Galerkin finite element methods (Cockburn et al., 2011). First, the local formulation promotes the parallelism of the algorithm; second, the assembly of a global mass matrix is not required, and so the memory is less demanding; third, in the case that one element is shared by more than one processor, we don't need to communicate the overlapping elements boundary condition between processors; finally, higher order elements can be implemented locally without concerning the compatibility with its neighbors, both *p*- and *h*-adaptive mesh refinement methods become more convenient to implement.

Although the shared elements in the coarse-grained domain lead to a lower parallel efficiency than the fully atomistics, it is worth noting that the parallel efficiency of coarse-graining is not the primary attractive feature of CAC, but rather its ability to extend the spatial scale under consideration to large dimensions, incorporating many body defect field interactions. This is quite difficult to achieve using standard MS methods.

References

Allen, M.P., Tildesley, D.J., 1989. Computer Simulation of Liquids. Oxford University Press, USA.
Beissel, S., Belytschko, T., 1996. Nodal integration of the element-free Galerkin method. Comput. Methods Appl. Mech. Eng. 139, 49–74.
Belytschko, T., Gracie, R., Ventura, G., 2009. A review of extended/generalized finite element methods for material modeling. Model. Simul. Mater. Sci. Eng. 17, 043001.
Bitzek, E., Koskinen, P., Ghler, F., Moseler, M., Gumbsch, P., 2006. Structural relaxation made simple. Phys. Rev. Lett. 97, 170201.
Biyikli, E., Yang, Q., To, A.C., 2014. Multiresolution molecular mechanics: dynamics. Comput. Methods Appl. Mech. Eng. 274, 42–55.
Bulatov, V., Cai, W., 2006. Computer Simulations of Dislocations. Oxford University Press, Oxford; New York.
Bulatov, V., Cai, W., Fier, J., Hiratani, M., Hommes, G., Pierce, T., Tang, M., Rhee, M., Yates, K., Arsenlis, T., 2004. Scalable line dynamics in ParaDiS. In: Proceedings of the 2004 ACM/IEEE Conference on Supercomputing, IEEE Computer Society, Washington, DC, USA, p. 19.
Chapra, S., Canale, R., 2009. Numerical Methods for Engineers, sixth ed. McGraw-Hill Science/Engineering/Math, Boston.
Chassagne, M., Legros, M., Rodney, D., 2011. Atomic-scale simulation of screw dislocation/coherent twin boundary interaction in Al, Au, Cu and Ni. Acta Mater. 59, 1456–1463.
Chen, Y., 2009. Reformulation of microscopic balance equations for multiscale materials modeling. J. Chem. Phys. 130, 134706.
Chen, Y., Lee, J., 2005. Atomistic formulation of a multiscale field theory for nano/micro solids. Philos. Mag. 85, 4095–4126.
Chen, Y., Lee, J.D., 2003a. Connecting molecular dynamics to micromorphic theory. (I). Instantaneous and averaged mechanical variables. Phys. A Stat. Mech. Appl. 322, 359–376.
Chen, Y., Lee, J.D., 2003b. Connecting molecular dynamics to micromorphic theory. (II). Balance laws. Phys. A Stat. Mech. Appl. 322, 377–392.
Chen, Y., Zimmerman, J., Krivtsov, A., McDowell, D.L., 2011. Assessment of atomistic coarse-graining methods. Int. J. Eng. Sci. 49, 1337–1349.
Cockburn, B., Karniadakis, G.E., Shu, C.W., 2011. Discontinuous Galerkin Methods: Theory, Computation and Applications. Springer (softcover reprint of the original 1st ed. 2000 edition).
Deng, Q., Chen, Y., 2013. A coarse-grained atomistic method for 3D dynamic fracture simulation. Int. J. Multiscale Comput. Eng 11, 227–237.
Deng, Q., Xiong, L., Chen, Y., 2010. Coarse-graining atomistic dynamics of brittle fracture by finite element method. Int. J. Plast. 26, 1402–1414.
Dewald, M.P., Curtin, W.A., 2007a. Multiscale modelling of dislocation/grain-boundary interactions: I. Edge dislocations impinging on Σ 11(113) tilt boundary in Al. Model. Simul. Mater. Sci. Eng. 15, S193.
Dewald, M.P., Curtin, W.A., 2007b. Multiscale modelling of dislocation/grain boundary interactions. II. Screw dislocations impinging on tilt boundaries in Al. Philos. Mag. 87, 4615–4641.
Dewald, M.P., Curtin, W.A., 2011. Multiscale modeling of dislocation/grain-boundary interactions: III. 60° dislocations impinging on Σ 3, Σ 9 and Σ 11 tilt boundaries in Al. Model. Simul. Mater. Sci. Eng. 19, 055002.
Dupuy, L.M., Tadmor, E.B., Miller, R.E., Phillips, R., 2005. Finite-temperature quasicontinuum: molecular dynamics without all the atoms. Phys. Rev. Lett. 95, 060202.
Dyka, C.T., Randles, P.W., Ingel, R.P., 1997. Stress points for tension instability in SPH. Int. J. Numer. Methods Eng 40, 2325–2341.
E, W., Ming, P., 2004. Analysis of multiscale methods. J. Comput. Math. 22, 210–219.
Hull, D., Bacon, D.J., 2011. Introduction to Dislocations, fifth ed. Butterworth-Heinemann.
Knap, J., Ortiz, M., 2001. An analysis of the quasicontinuum method. J. Mech. Phys. Solids 49, 1899–1923.
Kulkarni, Y., Knap, J., Ortiz, M., 2008. A variational approach to coarse graining of equilibrium and non-equilibrium atomistic description at finite temperature. J. Mech. Phys. Solids 56, 1417–1449.
Lin, P., 2003. Theoretical and numerical analysis for the quasi-continuum approximation of a material particle model. Math. Comput. 72, 657–675.
Lin, P., 2007. Convergence analysis of a quasicontinuum approximation for a two dimensional material without defects. SIAM J. Numer. Anal. 45, 313–332.
Luskin, M., Ortner, C., 2009. An analysis of node-based cluster summation rules in the quasicontinuum method. SIAM J. Numer. Anal. 47, 3070–3086.
Luskin, M., Ortner, C., 2013. Atomistic-to-continuum coupling. Acta Numer. 22, 397–508.
McDowell, D.L., 2010. A perspective on trends in multiscale plasticity. Int. J. Plast. 26, 1280–1309.
Miller, R.E., Tadmor, E.B., 2002. The quasicontinuum method: overview, applications and current directions. J. Comput. Aided Mater. Des. 9, 203–239.
Miller, R.E., Tadmor, E.B., 2009. A unified framework and performance benchmark of fourteen multiscale atomistic/continuum coupling methods. Model. Simul. Mater. Sci. Eng. 17, 053001.
Mishin, Y., Farkas, D., Mehl, M.J., Papaconstantopoulos, D.A., 1999. Interatomic potentials for monoatomic metals from experimental data and ab initio calculations. Phys. Rev. B 59, 3393–3407.
Mishin, Y., Mehl, M.J., Papaconstantopoulos, D.A., Voter, A.F., Kress, J.D., 2001. Structural stability and lattice defects in copper: Ab initio, tight-binding, and embedded-atom calculations. Phys. Rev. B 63, 224106.
Mott, P.H., Argon, A.S., Suter, U.W., 1992. The atomic strain tensor. J. Comput. Phys. 101, 140–150.
Park, J.Y., Im, S., 2008. Adaptive nonlocal quasicontinuum for deformations of curved crystalline structures. Phys. Rev. B 77, 184109.
Pearce, O., Gamblin, T., de Supinski, B.R., Arsenlis, T., Amato, N.M., 2014. Load balancing N-body simulations with highly non-uniform density. In: Proceedings of the 28th ACM International Conference on Supercomputing, ACM, New York, NY, USA, pp. 113–122.
Plimpton, S., 1995. Fast parallel algorithms for short-range molecular dynamics. J. Comput. Phys. 117, 1–19.
Qian, D., Gondhalekar, R.H., 2004. A virtual atom cluster approach to the mechanics of nanostructures. Int. J. Multiscale Comput. Eng 2, 277–290.
Rabczuk, T., Belytschko, T., Xiao, S., 2004. Stable particle methods based on Lagrangian kernels. Comput. Methods Appl. Mech. Eng. 193, 1035–1063.
Rudd, R., Broughton, J., 2000. Concurrent coupling of length scales in solid state systems. Phys. Status Solidi (b) 217, 251–291.
Schroeder, W., Martin, K., Lorensen, B., 2006. Visualization Toolkit: an Object-oriented Approach to 3D Graphics, fourth ed. Kitware.
Sheppard, D., Terrell, R., Henkelman, G., 2008. Optimization methods for finding minimum energy paths. J. Chem. Phys. 128, 134106.
Shilkrot, L., Miller, R.E., Curtin, W.A., 2004. Multiscale plasticity modeling: coupled atomistics and discrete dislocation mechanics. J. Mech. Phys. Solids 52, 755–787.
Shimizu, F., Ogata, S., Li, J., 2007. Theory of shear banding in metallic glasses and molecular dynamics calculations. Mater. Trans. 48, 2923–2927.
Shimokawa, T., Kinari, T., Shintaku, S., 2009. Adaptive mesh refinement with elastic stiffness coefficients in the quasicontinuum model. J. Comput. Sci. Tech. 3, 408–416.
Stukowski, A., 2010. Visualization and analysis of atomistic simulation data with OVITO—the open visualization tool. Model. Simul. Mater. Sci. Eng. 18, 015012.
Stukowski, A., Arsenlis, A., 2012. On the elastic plastic decomposition of crystal deformation at the atomic scale. Model. Simul. Mater. Sci. Eng. 20, 035012.
Stukowski, A., Bulatov, V.V., Arsenlis, A., 2012. Automated identification and indexing of dislocations in crystal interfaces. Model. Simul. Mater. Sci. Eng. 20, 085007.
Tadmor, E.B., Legoll, F., Kim, W.K., Dupuy, L.M., Miller, R.E., 2013. Finite-temperature quasi-continuum. Appl. Mech. Rev. 65, 010803.
Tadmor, E.B., Miller, R., 2012. Modeling Materials: Continuum, Atomistic and Multiscale Techniques. Cambridge University Press.

Tadmor, E.B., Ortiz, M., Phillips, R., 1996. Quasicontinuum analysis of defects in solids. Philos. Mag. A 73, 1529–1563.
Tang, S., Hou, T.Y., Liu, W.K., 2006. A mathematical framework of the bridging scale method. Int. J. Numer. Methods Eng. 65, 1688–1713.
Towns, J., Cockerill, T., Dahan, M., Foster, I., Gaither, K., Grimshaw, A., Hazlewood, V., Lathrop, S., Lifka, D., Peterson, G.D., Roskies, R., Scott, J.R., Wilkens-Diehr, N., 2014. XSEDE: accelerating scientific discovery. Comput. Sci. Eng. 16, 62–74.
Tsuru, T., Shibutani, Y., 2006. Atomistic simulations of elastic deformation and dislocation nucleation in Al under indentation-induced stress distribution. Model. Simul. Mater. Sci. Eng. 14, S55.
Van Koten, B., Luskin, M., 2011. Analysis of energy-based blended quasi-continuum approximations. SIAM J. Numer. Anal. 49, 2182–2209.
Van Swygenhoven, H., Derlet, P.M., Frøseth, A.G., 2004. Stacking fault energies and slip in nanocrystalline metals. Nat. Mater. 3, 399–403.
Verlet, L., 1967. Computer "experiments" on classical fluids. I. Thermodynamical properties of Lennard-Jones molecules. Phys. Rev. 159, 98–103.
Xiao, S.P., Belytschko, T., 2005. Material stability analysis of particle methods. Adv. Comput. Math. 23, 171–190.
Xiong, L., Chen, X., Zhang, N., McDowell, D.L., Chen, Y., 2014a. Prediction of phonon properties of 1D polyatomic systems using concurrent atomistic continuum simulation. Arch. Appl. Mech. 84, 1665–1675.
Xiong, L., Deng, Q., Tucker, G., McDowell, D.L., Chen, Y., 2012a. A concurrent scheme for passing dislocations from atomistic to continuum domains. Acta Mater. 60, 899–913.
Xiong, L., Deng, Q., Tucker, G.J., McDowell, D.L., Chen, Y., 2012b. Coarse-grained atomistic simulations of dislocations in Al, Ni and Cu crystals. Int. J. Plast. 38, 86–101.
Xiong, L., McDowell, D.L., Chen, Y., 2012c. Nucleation and growth of dislocation loops in Cu, Al and Si by a concurrent atomistic-continuum method. Scr. Mater. 67, 633–636.
Xiong, L., McDowell, D.L., Chen, Y., 2014b. Sub-THz phonon drag on dislocations by coarse-grained atomistic simulations. Int. J. Plast. 55, 268–278.
Xiong, L., Tucker, G., McDowell, D.L., Chen, Y., 2011. Coarse-grained atomistic simulation of dislocations. J. Mech. Phys. Solids 59, 160–177.
Xiong, L., Xu, S., McDowell, D.L., Chen, Y., 2015. Concurrent atomistic-continuum simulations of dislocation-void interactions in fcc crystals. Int. J. Plast. 65, 33–42.
Yang, Q., Biyikli, E., To, A.C., 2013a. Multiresolution molecular mechanics: statics. Comput. Methods Appl. Mech. Eng. 258, 26–38.
Yang, Q., Biyikli, E., To, A.C., 2014. Multiresolution molecular mechanics: convergence and error structure analysis. Comput. Methods Appl. Mech. Eng. 269, 20–45.
Yang, Q., Biyikli, E., Zhang, P., Tian, R., To, A.C., 2012. Atom collocation method. Comput. Methods Appl. Mech. Eng. 237–240, 67–77.
Yang, S., Chen, Y., 2015. Concurrent atomistic and continuum simulation of bi-crystal strontium titanate with tilt grain boundary. Proc. R. Soc. Lon A: Math. Phys. Eng. Sci. 471, 20140758.
Yang, S., Xiong, L., Deng, Q., Chen, Y., 2013b. Concurrent atomistic and continuum simulation of strontium titanate. Acta Mater. 61, 89–102.
Zhu, T., Li, J., Samanta, A., Leach, A., Gall, K., 2008. Temperature and strain-rate dependence of surface dislocation nucleation. Phys. Rev. Lett. 100, 025502.
Zimmerman, J.A., Bammann, D.J., Gao, H., 2009. Deformation gradients for continuum mechanical analysis of atomistic simulations. Int. J. Solids Struct. 46, 238–253.